https://doi.org/10.1016/j.ijheatmasstransfer.2018.01.139
This is the Pre-Published Version.

Lattice Boltzmann simulation of viscoplastic fluids on natural convection in an inclined enclosure with inner cold circular/elliptical cylinders (Part I: One cylinder)

GH. R. Kefayati *, H. Tang

Department of Mechanical Engineering, The Hong Kong Polytechnic University, Kowloon, Hong Kong SAR, China

Abstract

In this paper, natural convection in an inclined heated cavity with an inner cold circular/elliptical cylinder filled with viscoplastic fluids has been simulated by Lattice Boltzmann Method (LBM). In this study, the Bingham model without any regularization has been studied and moreover viscous dissipation effect has been analysed. Fluid flow, heat transfer, and yielded/unyielded parts have been conducted for certain pertinent parameters of Rayleigh number (Ra = 10^4, 10^5 and 10^6), the size of the inner cylinder, various inclined angles of the cavity (θ = 0°, 40°, 80°, 120°), the ratio of the inner cylinder radii (A = 0.25, 0.5, 1, 2, and 4), and different positions of the inner cylinder. Moreover, the Bingham number (Bn) is studied in a wide range of different studied parameters. Results indicate that the enhancement of the Rayleigh number augments the heat transfer, with a decrease in the size of the unyielded zones. For specific Rayleigh number and the position of the cylinder, the increase in the Bingham number declines the heat transfer and expands the unyielded sections between the inner cylinder and the enclosure. The rise of the cylinder size in the enclosure enhances heat transfer and develops the unyielded parts. The enhancement of the ratio of the inner cylinder radii augments the heat transfer and declines the unyielded sections. The movement of the cylinder from the center to the left and right sides horizontally enhances heat transfer in different Bingham numbers, and moreover, alters the size and shape of the unyielded zones. As the cylinder moves from the bottom to the top side of the cavity vertically, the heat transfer increases gradually while the yielded/unyielded zones change. The increase in the inclined angle of the enclosure alters the heat transfer and the yielded/unyielded zones noticeably. The rise of Eckert number even for higher range of practical values (Ec = 0.01, 0.1, and 1) alters the heat transfer and unyielded parts marginally, so the viscous dissipation term can be negligible in this study.

Key words: Viscoplastic fluid, Natural convection, LBM, Circular/elliptical

© 2018. This manuscript version is made available under the CC-BY-NC-ND 4.0 license http://creativecommons.org/licenses/by-nc-nd/4.0/.

1 Introduction

Natural convection of viscoplastic fluids in an enclosure due to its wide applications and interest in various chemical, metal, and food industries has been considered recently by researchers. Vola et al. [1] studied the natural convection in a cavity filled with a viscoplastic fluid using the Bingham model without any regularisation of the constitutive law. They applied a numerical method based on the combination of the characteristic/Galerkin method to cope with convection and of the Fortin–Glowinski decomposition/coordination method to deal with the non-differentiable and nonlinear terms that derive from the constitutive law. However, the streamlines and isotherms for various yield stress values were limited to one value of the Rayleigh number ($\mathrm{Ra} = 10^4$). Turan et al. [2] conducted a study into the simulations of natural convection in square enclosures filled with an incompressible Bingham fluid. The considered flow was laminar and steady. The commercial package FLUENT was utilised to solve the problem. In this study, a second-order central differencing scheme was used for the diffusive terms and a second order up-wind scheme for the convective terms. Coupling of the pressure and velocity fields was achieved using the SIMPLE algorithm. It should be noted that the default Bingham model in FLUENT is a bi viscosity model. The heat transfer and the flow velocities were investigated over a wide range of Rayleigh and Prandtl numbers. They found that the average Nusselt number augments with the rise of the Rayleigh number for both Newtonian and Bingham fluids, whereas the Nusselt numbers of Bingham fluids were smaller than those in Newtonian fluids for a fixed nominal Rayleigh number. They also mentioned that the mean Nusselt number of Bingham fluids decreased with an increase in the Bingham number. Moreover, it was observed that the conduction dominated regime occurs at large values of Bingham numbers. Finally, they reported that for low Bingham numbers, the mean Nusselt number increases with the enhancement of the Prandtl number; by contrast, the opposite behaviour was observed for large values of Bingham numbers. Turan et al. [3] continued their studies with analysing the effect of different aspect ratios (the ratio of the height to the length) of the cavity, adding to their previous results that the average Nusselt number follows a non-monotonic pattern with the aspect ratio for specific val-

* Corresponding author. Dr. Gholamreza Kefayati (GH. R. Kefayati)
Email addresses: gholamrezakefayati@gmail.com, gholamreza.kefayati@polyu.edu.hk (GH. R. Kefayati), h.tang@polyu.edu.hk (H. Tang).

ues of the Rayleigh and Prandtl numbers for both Newtonian and Bingham fluids. At small aspect ratios, the conduction is dominant whereas convection remains predominantly responsible for the heat transfer for large values of aspect ratios. In addition, it was found that the conduction dominated regime occurred at higher values of the Bingham numbers for increasing values of the aspect ratio for a given value of the Rayleigh number. Turan et al. [4] scrutinised the laminar Rayleigh-Bnard convection of yield stress fluids in a square enclosure. The applied method and the achieved results were similar to the two previous studies. Huilgol and Kefayati [5] studied natural convection in a square cavity with differentially heated vertical sides and filled with a Bingham fluid without any regularisation. The finite element method (FEM) based on the operator splitting method was utilised to solve the problem. It was observed that for specific Rayleigh and Prandtl numbers, the increase in the Bingham number decreases the heat transfer. Furthermore, it was found that the growth of the Bingham number expands the unyielded sections in the cavity. Finally, they mentioned that for fixed Rayleigh and Bingham numbers, the unyielded regions grow with the augmentation of the Prandtl number. Karimfazli et al. [6] explored the feasibility of a novel method for the regulation of heat transfer across a cavity. They used computational simulations to resolve the Navier-Stokes and energy equations for different yield stresses.

Many studies have conducted the effect of the presence of the body inside the enclosure on the natural convection of Newtonian fluids and focused on the diverse body shapes such as circular, square and triangular cylinders [7–14]. Just recently, natural convection of viscoplastic fluids is investigated, using regularized models inside cavities with hot and cold bodies. Baranwal and Chhabra [15] studied laminar natural convection heat transfer to Bingham plastic fluids from two differentially heated isothermal cylinders confined in a square enclosure. They utilized regularization approaches of bi–viscosity, the Bercovier and Engelman models. They used the finite element method-based solver, COMSOL Multiphysics (version 4.3a) to solve the governing equations. Dutta et al. [16] investigated the effects of tilt angle and fluid yield stress on the laminar natural convection from an isothermal square cylinder in a Bingham plastic fluid confined in a square duct. They also applied the same regularization approaches of bi–viscosity, the Bercovier and Engelman models. They also applied the finite element method-based solver, COMSOL Multiphysics (version 4.3a) to solve the governing equations.

Lattice Boltzmann method (LBM) has been demonstrated to be a very effective mesoscopic numerical method to model a broad variety of complex fluid flow phenomena [17–28]. Lattice Boltzmann method (LBM) combined with Finite Difference Method (FDM) has been applied for this problem [29]. It was demonstrated to be a successful mesoscopic method for simulation of Non-Newtonian fluids. Independency of the method to the relaxation time in contrast with common LBM provokes the method to solve different non-

Newtonian fluid energy equations successfully as the method protects the positive points of LBM simultaneously. Huilgol and Kefayati [30] explained and derived the two and three dimensional equations of continuum mechanics for this method and demonstrated that the theoretical development can be applied to all fluids, whether they be Newtonian, or power law fluids, or viscoelastic and viscoplastic fluids. Following the previous study, Huilgol and Kefayati [31] derived the two and three dimensional equations of this method for the cartesian, cylindrical and spherical coordinates. Double-diffusive natural convection of non-Newtonian power-law fluid in a square cavity was studied by the cited method while entropy generations through fluid friction, heat transfer, and mass transfer were analyzed [32]. In the following study, heat and mass transfer as well as entropy generations in natural convection of non-Newtonian power-law fluids in an inclined porous cavity were studied, applying the method [33,34]. Kefayati and Huilgol [35] applied this method to simulate the steady flow in a pipe of square cross-section when the pipe is filled with a Bingham fluid. The problem was solved employing the Bingham model without any regularisation. In the next step, Kefayati and Huilgol [36] utilized the mesoscopic method to conduct a two-dimensional simulation of steady mixed convection in a square enclosure with differentially heated sidewalls when the enclosure is filled with a Bingham fluid. The problem was solved by the Bingham model without any regularisations and also by applying the regularised Papanatasiou model. Double-diffusive natural convection and entropy generations of Bingham fluid in a square cavity and open cavities were simulated by this method [37,38]. Double-diffusive natural convection and entropy generations, studying Soret and Dufour effects and viscous dissipation in a heated enclosure with an inner cold cylinder filled with non-Newtonian Carreau fluid were simulated by the method [39,40].

The main aim of this study is to simulate natural convection of Bingham fluid in a heated cavity with an inner cold cylinder as the yielded/unyielded sections have been displayed. In this study, the Bingham model without any regularization has been studied and moreover viscous dissipation effect also has been analyzed. LBM has been employed to study the problem numerically. Moreover, it is endeavored to express the effects of different parameters on heat transfer as well as yielded/unyielded zones. The obtained results were validated with previous numerical investigations and the effects of the main parameters (Rayleigh number, Bingham number, Eckert number, the size and position of the cold cylinder) on unyielded parts and heat transfer are researched.

2 Theoretical formulation

2.1 Problem statement

The geometry of the present problem is shown in Fig.1. The temperature of the enclosure walls have been considered to be maintained at high temperature of T_H as the inner cylinder is kept at low temperature of T_C. The lengths of the enclosure sidewalls are L where the cylinder center is defined by (x_c, y_c). The angle between the x direction and the bottom side of the cavity (θ) is altered counterclockwise. The inner circular/elliptical cylinder has the horizontal radius (a), the vertical radius (b), and the ratio of radii (A = b/a). The cavity is filled with a viscoplastic fluid. The prandtl number is fixed at Pr=0.1. There is no heat generation and thermal radiation. The flow is incompressible, and laminar. The density variation is approximated by the standard Boussinesq model for temperature. The viscous dissipation in the energy equation has been analyzed in this study.

2.2 Dimensional equations

Based on the above assumptions, and applying the Boussinesq approximation, the mass, momentum, and energy equations are [35,36]:

$$\frac{\partial u}{\partial x} + \frac{\partial v}{\partial y} = 0, \tag{2.1}$$

$$\rho\left(\frac{\partial u}{\partial t} + u\frac{\partial u}{\partial x} + v\frac{\partial u}{\partial y}\right) = -\frac{\partial p}{\partial x} + \left(\frac{\partial \tau_{xx}}{\partial x} + \frac{\partial \tau_{xy}}{\partial y}\right) + g\rho sin\theta\left[1 + \beta_T(T - T_C)\right], \tag{2.2}$$

$$\rho\left(\frac{\partial v}{\partial t} + u\frac{\partial v}{\partial x} + v\frac{\partial v}{\partial y}\right) = -\frac{\partial p}{\partial y} + \left(\frac{\partial \tau_{yy}}{\partial y} + \frac{\partial \tau_{xy}}{\partial x}\right) + g\rho cos\theta\left[1 + \beta_T(T - T_C)\right], \tag{2.3}$$

In the above equations, ($\mathbf{x} = x\,\mathbf{i} + y\,\mathbf{j}$), t, $\boldsymbol{\tau}$ are the Cartesian coordinates, time, and shear stress; respectively. In addition, ($\mathbf{u} = u\,\mathbf{i} + v\,\mathbf{j}$), T, ρ, and g are the dimensional velocities, temperature, density, and gravity acceleration; respectively. β_T is the coefficient of thermal expansion and ρ is density. Now,

let the pressure p be written as the sum $p = p_s + p_d$, where the static part p_s accounts for gravity alone, and p_d is the dynamic part. Thus,

$$-\frac{\partial p_s}{\partial \mathbf{x}} = \rho g \left(sin\theta\, \mathbf{i} + cos\theta\, \mathbf{j}\right)\cdot \tag{2.4}$$

$$\frac{\partial T}{\partial t}+u\frac{\partial T}{\partial x}+v\frac{\partial T}{\partial y} = \alpha\left(\frac{\partial^2 T}{\partial x^2}+\frac{\partial^2 T}{\partial y^2}\right)+\frac{1}{\rho c_p}\left[\tau_{xx}\left(\frac{\partial u}{\partial x}\right)+\tau_{xy}\left(\frac{\partial u}{\partial y}+\frac{\partial v}{\partial x}\right)+\tau_{yy}\left(\frac{\partial v}{\partial y}\right)\right] \tag{2.5}$$

α and c_p are the thermal diffusivity and the specific heat at constant pressure, respectively [41–45].

2.3 Constitutive model

Bingham [46] constituted the viscoplastic fluids as follows:

$$\begin{cases} \mathbf{A}(\mathbf{u}) = \mathbf{0}, & K(\boldsymbol{\tau}) \leq \tau_y, \\ \boldsymbol{\tau} = \left(\eta + \frac{\tau_y}{K(\mathbf{u})}\right)\mathbf{A}(\mathbf{u}), & K(\boldsymbol{\tau}) > \tau_y, \end{cases} \tag{2.6}$$

where the viscosity η and the yield stress τ_y are constant, and the two invariants $K(\mathbf{u})$ and $K(\boldsymbol{\tau})$ are defined below:

$$2K^2(\mathbf{u}) = \mathbf{A}(\mathbf{u}) : \mathbf{A}(\mathbf{u}), \quad 2K^2(\boldsymbol{\tau}) = \boldsymbol{\tau} : \boldsymbol{\tau}. \tag{2.7}$$

where

$$\mathbf{A}(\mathbf{u}) = \nabla\mathbf{u} + \nabla\mathbf{u}^T. \tag{2.8}$$

Due to the discontinuity in the Bingham model, approximate models such as the Papanastasiou [47], Bercovier and Engelman [48], and the bi-viscosity [49] models are used by researchers and different software packages. However, a constitutive equation for a Bingham fluid fully equivalent to the original form can be used. This method was proposed and developed by Duvaut and Lions [50] and Glowinski [51] and the constitutive equation takes the form

$$\boldsymbol{\tau} = \eta\mathbf{A}(\mathbf{u}) + \sqrt{2}\,\tau_y\,\boldsymbol{\Lambda}, \quad \mathbf{1} : \boldsymbol{\Lambda} = 0, \tag{2.9}$$

where one may call the second order, symmetric, tensor $\boldsymbol{\Lambda}$ the *viscoplasticity constraint tensor*. Note that the traceless condition $\mathbf{1} : \boldsymbol{\Lambda} = 0$ has been imposed on this tensor so that the stress tensor $\boldsymbol{\tau}$ satisfies the condition tr $\boldsymbol{\tau} = 0$. In

order to demarcate the flow field into unyielded/yielded zones, one requires that the tensor $\mathbf{\Lambda}$ meet the following conditions:

$$\mathbf{\Lambda} : \mathbf{\Lambda} = \begin{cases} < 1, & \mathbf{A}(\mathbf{u}) = \mathbf{0}, \\ 1, & \mathbf{A}(\mathbf{u}) \neq \mathbf{0}. \end{cases} \tag{2.10}$$

These conditions satisfy those imposed on the stress tensor, viz., $K(\boldsymbol{\tau}) \leq \tau_y$ when $\mathbf{A}(\mathbf{u}) = \mathbf{0}$, and $\tau_y < K(\boldsymbol{\tau})$ when $\mathbf{A}(\mathbf{u}) \neq \mathbf{0}$. The problem of determining where the flow is rigid and where it is liquid-like has been shifted to finding the tensor $\mathbf{\Lambda}$ in the flow field such that is satisfies Eq.(2.10). What has been proposed is important for the following reasons:

(1) The constitutive equations Eqs. (2.9) - (2.10) are defined over the entire flow domain, not just where the fluid has yielded.
(2) One searches for the solution velocity field $\mathbf{u}$ and the viscoplasticity constraint tensor $\mathbf{\Lambda}$ to determine the yielded/unyielded regions. There are no singularities because one is not trying to find the location of the yield surface(s) through the limit of $\mathbf{A}(\mathbf{u})/K(\mathbf{u})$ as $\mathbf{A}(\mathbf{u}) \to \mathbf{0}$.
(3) However, the equations of motion now involve two unknown fields: a vector field $\mathbf{u}$, and a symmetric tensor field $\mathbf{\Lambda}$. The latter requires that there should exist a connection between the velocity field $\mathbf{u}$ and $\mathbf{\Lambda}$. Under Dirichlet boundary conditions, it is possible to prove such a relation. Here, we provide a summary of the results.
$\mathbf{\Lambda}$ can be obtained from a simple projection operation as follows [5,35,36]:

$$\mathbf{\Lambda} = P_{\mathcal{M}}\Big(\mathbf{\Lambda} + r\tau_y \mathbf{A}(\mathbf{v})\Big), \quad \forall r > 0, \tag{2.11}$$

where $\mathcal{M} = \{\boldsymbol{\mu} | \boldsymbol{\mu} = (\mu_{ij})_{1 \leq i,j \leq 2} \in (L^2(\Omega))^4, \|\boldsymbol{\mu}\| \leq 1 \text{ a.e. on } \Omega\}$ and

$$P_{\mathcal{M}} : (L^2(\Omega))^4 \to \mathcal{M} \tag{2.12}$$

is the projection operator defined so that $P_{\mathcal{M}}(\boldsymbol{\mu}) = \boldsymbol{\mu}$, if $\|\boldsymbol{\mu}\| \leq 1$, and $P_{\mathcal{M}}(\boldsymbol{\mu}) = \boldsymbol{\mu}/\|\boldsymbol{\mu}\|$ otherwise. Note that in the context of Eq. (2.11), the tensor $\boldsymbol{\mu} = \mathbf{\Lambda} + r\tau_y \mathbf{A}(\mathbf{v})$ and it is symmetric. Further, the tensor $\boldsymbol{\mu}$ must be dimensionless for $\mathbf{\Lambda}$ is also dimensionless.

where $r > 0$ is a real number to be specified. Successive iterations are performed till convergence is achieved to the desired level of accuracy. Note that the yield surface is the boundary between $||\mathbf{\Lambda}|| < 1$ and $||\mathbf{\Lambda}|| = 1$. Hence, the solution of the boundary value problem delivers in the limit both the velocity field as well as the shape and location of the yield surface.

2.4 Boundary conditions

The flow domain is given by $\omega = (0, L) \times (0, L)$, and the boundary $\Gamma = \partial\omega$. It is the union of five disjoint subsets:

$$\Gamma_1 = \{(x, y), x = 0, 0 \leq y \leq L\}, \tag{2.13a}$$

$$\Gamma_2 = \{(x, y), x = L, 0 \leq y \leq L\}, \tag{2.13b}$$

$$\Gamma_3 = \{(x, y), 0 \leq x \leq L, y = 0\}, \tag{2.13c}$$

$$\Gamma_4 = \{(x, y), 0 \leq x \leq L, y = L\}, \tag{2.13d}$$

$$\Gamma_5 = \left\{(x, y), \frac{(x - x_c)^2}{a^2} + \frac{(y - y_c)^2}{b^2} = 1\right\}. \tag{2.13e}$$

x_c and y_c are the horizontal and vertical positions of the cylinder center. The parameters of a and b are the horizontal and vertical radii of the inner cylinder.

The boundary condition for the velocity is straightforward:

$$\mathbf{u}|_{\Gamma_1} = \mathbf{u}|_{\Gamma_2} = \mathbf{u}|_{\Gamma_3} = \mathbf{u}|_{\Gamma_4} = \mathbf{u}|_{\Gamma_5} = \mathbf{0}. \tag{2.14}$$

The boundary conditions for the temperature and concentration are:

$$T|_{\Gamma_1} = T|_{\Gamma_2} = T|_{\Gamma_3} = T|_{\Gamma_4} = T_H, \quad T|_{\Gamma_5} = T_C \tag{2.15}$$

2.5 Non-dimensional equations

We define the buoyancy velocity scale $U = \left(\frac{\alpha}{L}\right) Ra^{0.5}$ where Ra is the Rayleigh number. In order to proceed to the numerical solution of the system, the following non dimensional variables are introduced [52].

$$t^* = \frac{t\,U}{L}, \quad x^* = x/L, \quad y^* = y/L, \quad \mathbf{u}^* = \frac{\mathbf{u}}{U}, \quad {p_d}^* = \frac{p_d}{\rho\,U^2}, \tag{2.16}$$

$$T^* = (T - T_C)/\Delta T, \quad \Delta T = T_H - T_C, \quad \boldsymbol{\tau}^* = \frac{\sqrt{2}\,\boldsymbol{\tau}\,L}{\eta\,U} \tag{2.17}$$

By substitution of Eqs. (2.16) - (2.17) into Eqs. (2.1) - (2.5) and dropping asterisks, the following system of non-dimensional equations are derived:

$$\frac{\partial u}{\partial x} + \frac{\partial v}{\partial y} = 0 \tag{2.18}$$

$$\frac{\partial u}{\partial t} + u\frac{\partial u}{\partial x} + v\frac{\partial u}{\partial y} = -\frac{\partial p_d}{\partial x} + \frac{Pr}{\sqrt{\mathrm{Ra}}}\left(\frac{\partial \tau_{xx}}{\partial x} + \frac{\partial \tau_{xy}}{\partial y}\right) + \mathrm{Pr}\; T sin\theta \tag{2.19}$$

$$\frac{\partial v}{\partial t} + u\frac{\partial v}{\partial x} + v\frac{\partial v}{\partial y} = -\frac{\partial p_d}{\partial y} + \frac{Pr}{\sqrt{\mathrm{Ra}}}\left(\frac{\partial \tau_{xy}}{\partial x} + \frac{\partial \tau_{yy}}{\partial y}\right) + \mathrm{Pr}\ T cos\theta \quad (2.20)$$

$$\begin{aligned} \frac{\partial T}{\partial t} + u\frac{\partial T}{\partial x} + v\frac{\partial T}{\partial y} &= \frac{1}{\sqrt{Ra}}\left(\frac{\partial^2 T}{\partial x^2} + \frac{\partial^2 T}{\partial y^2}\right) \\ +\frac{Pr\ Ec}{\sqrt{Ra}} &\left[\tau_{xx}\left(\frac{\partial u}{\partial x}\right) + \tau_{xy}\left(\frac{\partial u}{\partial y} + \frac{\partial v}{\partial x}\right) + \tau_{yy}\left(\frac{\partial v}{\partial y}\right)\right] \end{aligned} \quad (2.21)$$

In the case of the exact Bingham model [35,36], the non-dimensional stresses are given by

$$\tau_{xx} = \left[2\left(\frac{\partial u}{\partial x}\right) + \ \mathrm{Bn}\ \Lambda_{xx}\right] \ , \quad (2.22a)$$

$$\tau_{yy} = \left[2\left(\frac{\partial v}{\partial y}\right) + \ \mathrm{Bn}\ \Lambda_{yy}\right] \ , \quad (2.22b)$$

$$\tau_{xy} = \left[\left(\frac{\partial u}{\partial y} + \frac{\partial v}{\partial x}\right) + \ \mathrm{Bn}\ \Lambda_{xy}\right] \ , \quad (2.22c)$$

$$\mathbf{\Lambda}^{n+1} = P_{\mathcal{M}}\Big(\mathbf{\Lambda}^n + \mathrm{Pr}\ \mathrm{Bn}\ \mathbf{A}(\mathbf{u})^n\Big), \quad (2.22d)$$

The mentioned non-dimensional parameters in the above equations are as follows:

Rayleigh number:

$$Ra = \frac{\rho\,\beta_T\,g L^3 \Delta T}{\eta\,\alpha} \quad (2.23)$$

Prandtl number:

$$\mathrm{Pr} = \frac{\eta}{\rho\,\alpha} \ , \quad (2.24)$$

Bingham number:

$$Bn = \frac{\sqrt{2}\,\tau_y\,L}{\eta\,U} \ , \quad (2.25)$$

Eckert number:

$$Ec = \frac{U^2}{c_p\,\Delta T}\,, \quad (2.26)$$

Since the buoyancy velocity scale is $U = \left(\frac{\alpha}{L}\right)\ Ra^{0.5}$, ΔT and L are equal to unity, the Eckert number has the following relation to the specific heat at constant pressure, Rayleigh number, and thermal diffusivity

$$Ec \propto \frac{\alpha^2\,Ra}{c_p}\,, \quad (2.27)$$

The α and c_p for different viscoplastic fluids in various temperatures can be ranged over (10^{-3} – 10^{-6} m^2/s) and (10^2 – 10^4 J/kg K). So, in the highest studied Rayleigh numbers ($Ra = 10^6$), and the thermal diffusivity ($\alpha = 10^{-3}$) as well as the lowest value of the specific heat at constant pressure, $c_p = 10^3$, the highest amount of the Eckert number would be Ec = 0.01. Therefore, the Eckert number in practical view would be in the range of Ec $\ll$ 0.01. From the Eq.(2.21), it can be observed the viscous dissipation term (The last term in the right side of the equation) is too small and negligible. However, some simulations are conducted to prove the cited theorem which the viscous dissipation is negligible. We have analysed the Eckert number in a higher range at Ec = 0.01, 0.1 and 1 to observe the viscous dissipation term effect on heat transfer, and yielded/unyielded parts.

The local and the average Nusselt numbers at the cavity sides are as

$$Nu = \left(-\frac{\partial T}{\partial r}\right)_{r=0}, \tag{2.28a}$$

$$Nu_{avg} = \int_0^1 Nu\, ds, \, . \tag{2.28b}$$

where r denotes the unit normal direction on a specific side wall s.
The total average Nusselt numbers are as

$$Nu_{tot_{avg}} = Nu_{L_{avg}} + Nu_{R_{avg}} + Nu_{B_{avg}} + Nu_{T_{avg}} \tag{2.29}$$

In the above equation, the subscribes of tot, L, R, B, T, avg means total, the left wall of the cavity, the right wall of the cavity, the bottom wall of the cavity, the top wall of the cavity, and average; respectively.

3 The numerical method

The LBM equations and their relationships with continuum equations have been explained in details in Huilgol and Kefayati [30]. Here, just a brief description about the main equations would be cited. In addition, the applied algorithm has been described and the studied problem equations in the LBM are mentioned.

3.1 The Continuity and Momentum equations

To have the continuity and momentum equations, a discrete particle distribution function f_α is defined over a D2Q9 lattice where it should satisfy an evolution equation:

$$\frac{\partial f_\alpha}{\partial t} + \boldsymbol{\xi}_\alpha \cdot \nabla_{\mathbf{x}} f_\alpha - F_\alpha = -\frac{1}{\varepsilon\ \phi}(f_\alpha - f_\alpha^{eq}), \tag{3.1}$$

where ε is a small parameter to be prescribed when numerical simulations are considered. ϕ is the relaxation time.

Associated to each node is a lattice velocity vector $\boldsymbol{\xi}_\alpha$. It is defined as follows:

$$\boldsymbol{\xi}_\alpha = \begin{cases} (0,0), & \alpha = 0, \\ \sigma(\cos\Theta_\alpha, \sin\Theta_\alpha) & \alpha = 1,3,5,7, \\ \sigma\sqrt{2}(\cos\Theta_\alpha, \sin\Theta_\alpha), & \alpha = 2,4,6,8. \end{cases} \tag{3.2}$$

Here, the angles Θ_α are defined through $\Theta_\alpha = (\alpha - 1)\pi/4,\ \alpha = 1, \cdots, 8$. The constant σ has to be chosen with care for it affects numerical stability; its choice depends on the problem. The method for finding the parameter σ which satisfies the Courant-Friedrichs-Lewy (CFL) condition is described in [30].

The equilibrium distribution function, f_α^{eq}, is different from the conventional ones adopted by previous researchers, who normally expand the Maxwellian distribution function. In the present approach, we expand f_α^{eq} as a quadratic in terms of $\boldsymbol{\xi}_\alpha$, using the notation of linear algebra [30,31]:

$$f_\alpha^{eq} = A_\alpha + \boldsymbol{\xi}_\alpha \cdot \mathbf{B}_\alpha + (\boldsymbol{\xi}_\alpha \otimes \boldsymbol{\xi}_\alpha) : \mathbf{C}_\alpha,\ \alpha = 0, 1, 2, \cdots, 8. \tag{3.3}$$

The relation between the above parameters and non-dimensional macroscopic values are as follows:

$$A_0 = \rho - \frac{2p}{\sigma^2} - \frac{\rho|\mathbf{u}|^2}{\sigma^2} + \frac{Pr}{\sqrt{Ra}}\left(\frac{\tau_{xx} + \tau_{yy}}{2}\right), \quad A_\alpha = 0,\ \alpha = 1, 2, \cdots, 8. \tag{3.4}$$

$$\mathbf{B}_1 = \frac{\rho\mathbf{u}}{2\sigma^2} = \mathbf{B}_\alpha,\ \alpha = 1,3,5,7; \quad \mathbf{B}_\alpha = \mathbf{0},\ \alpha = 0,2,4,6,8. \tag{3.5}$$

Next, the matrices $\mathbf{C}_\alpha$ are such that $\mathbf{C}_0 = 0;\ \mathbf{C}_1 = \mathbf{C}_\alpha,\ \alpha = 1,3,5,7;\ \mathbf{C}_2 = \mathbf{C}_\alpha,\ \alpha = 2,4,6,8$, where

$$\mathbf{C}_1 = \begin{bmatrix} C_{11} & 0 \\ 0 & C_{22} \end{bmatrix}, \quad C_{11} = \frac{1}{2\sigma^4}\left(p + \rho u^2 - \frac{Pr}{\sqrt{Ra}}\,\tau_{xx}\right), \quad C_{22} = \frac{1}{2\sigma^4}\left(p + \rho v^2 - \frac{Pr}{\sqrt{Ra}}\,\tau_{yy}\right), \tag{3.6}$$

$$\mathbf{C}_2 = \begin{bmatrix} 0 & C_{12} \\ C_{21} & 0 \end{bmatrix}, \quad C_{12} = C_{21} = \frac{1}{8\sigma^4}\left(\rho uv - \frac{Pr}{\sqrt{Ra}}\,\tau_{xy}\right). \tag{3.7}$$

The body force term F_α in (3.1) can be defined as

$$F_\alpha = 0, \quad \alpha = 0, 2, 4, 6, 8, \tag{3.8a}$$

$$F_\alpha = \frac{1}{2\sigma^2}\mathbf{N}\cdot\boldsymbol{\xi}_\alpha, \quad \alpha = 1, 3, 5, 7 \tag{3.8b}$$

where

$$\mathbf{N} = \Pr\, T\,(sin\theta\,\mathbf{i} + cos\theta\,\mathbf{j}) \tag{3.9}$$

The main equations of the discrete particle distribution function (3.1) is solved by the splitting method of Toro [53]. Hence, the equations can be separated into two parts. The first one is the streaming section which is written as

$$\frac{\partial f_\alpha}{\partial t} + \boldsymbol{\xi}_\alpha \cdot \nabla_{\mathbf{x}} f_\alpha - F_\alpha = 0. \tag{3.10}$$

Eqs.(3.10) has been solved with the method of Lax and Wendroff [54] and the following equations are used.

$$\begin{aligned} f_\alpha^{n+1}(i,j) = f_\alpha^n(i,j) &- \frac{\Delta t}{2\Delta x}\xi_\alpha(i)\left[f_\alpha^n(i+1,j) - f_\alpha^n(i-1,j)\right] \\ &- \frac{\Delta t}{2\Delta y}\xi_\alpha(j)\left[f_\alpha^n(i,j+1) - f_\alpha^n(i,j-1)\right] + \\ \frac{\Delta t^2}{2\Delta x^2}{\xi_\alpha}^2(i)&\left[f_\alpha^n(i+1,j) - 2f_\alpha^n(i,j) + f_\alpha^n(i-1,j)\right] + F_\alpha(i)\Delta t + \\ \frac{\Delta t^2}{2\Delta y^2}{\xi_\alpha}^2(j)&\left[f_\alpha^n(i,j+1) - 2f_\alpha^n(i,j) + f_\alpha^n(i,j-1)\right] + F_\alpha(j)\Delta t\ , \end{aligned} \tag{3.11}$$

In Eqs.(3.11), we have put

$$\xi_\alpha(i) = \boldsymbol{\xi}_\alpha\cdot\mathbf{i}, \quad \xi_\alpha(j) = \boldsymbol{\xi}_\alpha\cdot\mathbf{j}, \quad F_\alpha(i) = \mathbf{F}_\alpha\cdot\mathbf{i}, \quad F_\alpha(j) = \mathbf{F}_\alpha\cdot\mathbf{j}. \tag{3.12}$$

The second part is the collision section which is as follows:

$$\frac{\partial f_\alpha}{\partial t} = -\frac{1}{\varepsilon\phi}(f_\alpha(\mathbf{x},t) - f_\alpha^{eq}(\mathbf{x},t)), \tag{3.13}$$

Eqs.(3.13) can be solved by using the Euler method and the choice of $\varepsilon\phi$ is taken as the time step (Δt). That is

$$\frac{f_\alpha(\mathbf{x},t+\Delta t) - f_\alpha(\mathbf{x},t)}{\Delta t} = -\frac{1}{\varepsilon\phi}(f_\alpha(\mathbf{x},t) - f_\alpha^{eq}(\mathbf{x},t)), \tag{3.14}$$

from which one obtains

$$f_\alpha(\mathbf{x},t+\Delta t) = f_\alpha^{eq}(\mathbf{x},t), \tag{3.15}$$

3.2 The Energy Equation

In order to obtain the energy equation, an internal energy distribution function g_α is introduced and it is assumed to satisfy an evolution equation similar to that for f_α. Thus,

$$\frac{\partial g_\alpha}{\partial t} + \boldsymbol{\xi}_\alpha \cdot \nabla_{\mathbf{x}} g_\alpha - G_\alpha = -\frac{1}{\varepsilon\phi}(g_\alpha - g_\alpha^{eq}). \tag{3.16}$$

G_α refers to the external supply e.g. radiation in the energy equation. Here, g_α^{eq} has a monomial expansion:

$$g_\alpha^{eq} = D_\alpha + \boldsymbol{\xi}_\alpha \cdot \mathbf{E}_\alpha, \tag{3.17}$$

One way of satisfying the above is to assume, as before, that the scalars are given by $D_\alpha = D_1,\ \alpha = 1, 3, 5, 7$, and $D_\alpha = D_2,\ \alpha = 2, 4, 6, 8,$. In this problem, the non-dimensional parameters are obtained as follows (See Eqs. 3.39,3.42 in Huilgol and Kefayati [30]):

$$D_0 = T, \quad D_1 = 0, \quad D_2 = 0. \tag{3.18}$$

Regarding the vectors, it is assumed that $\mathbf{E}_0 = \mathbf{0},\ \mathbf{E}_\alpha = \mathbf{E}_1,\ \alpha = 1, 3, 5, 7; \mathbf{E}_\alpha = \mathbf{E}_2,\ \alpha = 2, 4, 6, 8$, where (See Eqs. 3.40,3.43 in Huilgol and Kefayati [30])

$$\mathbf{E}_1 = \frac{\left[\mathbf{u}\,T - \frac{1}{\sqrt{Ra}}\frac{\partial T}{\partial \mathbf{x}} - \frac{Pr\,Ec}{\sqrt{Ra}}\ \left[(u\,\tau_{xx} + v\,\tau_{xy}) + (u\,\tau_{yx} + v\,\tau_{yy})\right]\right]}{2\,\sigma^2}. \tag{3.19}$$

Finally, $G_\alpha = 0$.

The main equations of the internal energy distribution function are solved by the splitting method of Toro [53]. Hence, the equations can be separated into two parts. The first one is the streaming section which is written as

$$\frac{\partial g_\alpha}{\partial t} + \boldsymbol{\xi}_\alpha \cdot \nabla_{\mathbf{x}} g_\alpha = 0. \tag{3.20}$$

Eqs.(3.20) have been solved with the method of Lax and Wendroff [54] and the following equations are used.

$$g_\alpha^{n+1}(i,j) = g_\alpha^n(i,j) - \frac{\Delta t}{2\Delta x}\xi_\alpha(i)\left[g_\alpha^n(i+1,j) - g_\alpha^n(i-1,j)\right] - \frac{\Delta t}{2\Delta y}\xi_\alpha(j)\left[g_\alpha^n(i,j+1) - g_\alpha^n(i,j-1)\right] + \frac{\Delta t^2}{2\Delta x^2}{\xi_\alpha}^2(i)\left[g_\alpha^n(i+1,j) - 2g_\alpha^n(i,j) + g_\alpha^n(i-1,j)\right] + \frac{\Delta t^2}{2\Delta y^2}{\xi_\alpha}^2(j)\left[g_\alpha^n(i,j+1) - 2g_\alpha^n(i,j) + g_\alpha^n(i,j-1)\right] \quad (3.21)$$

The second part is the collision section which is as follows:

$$\frac{\partial g_\alpha}{\partial t} = -\frac{1}{\varepsilon\phi}(g_\alpha(\mathbf{x},t) - g_\alpha^{eq}(\mathbf{x},t)). \quad (3.22)$$

Eqs.(3.22) can be solved by using the Euler method and the choice of $\varepsilon\phi$ is taken as the time step (Δt). That is

$$\frac{g_\alpha(\mathbf{x},t+\Delta t) - g_\alpha(\mathbf{x},t)}{\Delta t} = -\frac{1}{\varepsilon\phi}(g_\alpha(\mathbf{x},t) - g_\alpha^{eq}(\mathbf{x},t)), \quad (3.23)$$

from which one obtains

$$g_\alpha(\mathbf{x},t+\Delta t) = g_\alpha^{eq}(\mathbf{x},t). \quad (3.24)$$

3.3 Boundary conditions

One of the main advantages of the current approach is that boundary conditions can be incorporated in a manner similar to macroscopic methods, in contrast with other methods utilised for solving LBM equations. The latter employ complicated special relationships for the discrete particle distribution function (f_α) and the internal energy distribution function (g_α) for each kind of boundary conditions and problems [55,56]. For example, methods such as on-grid and mid-grid bounce back are used when the velocity is zero on the boundary; when the boundary is in motion, bounce-back is used along with a set of linear equations to determine the boundary values f_α. In the method used here, the boundary conditions of f_α and g_α can be obtained directly from the macroscopic values on the boundaries due to the relationships of the macroscopic values with f_α and g_α. As a result, in this method, boundary conditions, especially the Dirichlet conditions, can be included in various problems similar to macroscopic methods and no special equations for f_α and g_α are needed to incorporate the boundary conditions. Therefore, we apply the cited macroscopic values (velocities and temperatures) on the boundary conditions in the Eqs. (2.13a)–(2.13e) on the cited boundaries Eqs. (2.14),(2.15) directly. In addition, for the curved boundaries, just we need to employ the curved equations Eqs. (2.13e) in the Cartesian coordinates.

4 Applied parameters, code validation and grid independence

Lattice Boltzmann Method (LBM) scheme is utilized to simulate laminar natural convection in a heated enclosure with an inner cold cylinder that is filled with a viscoplastic fluid in the presence of the viscous dissipation in the energy equation. The Prandtl number is fixed at Pr=0.1. This problem is investigated at different parameters of Rayleigh number (Ra = 10^4, 10^5 and 10^6), the size of the inner cylinder, various inclined angles of the cavity ($\theta = 0°$, 40°, 80°, 120°), the ratio of the inner cylinder radii (A = 0.25, 0.5, 1, 2, and 4), different positions of the inner cylinder and Eckert number (Ec = 0.01, 0.1, and 1). Moreover, the Bingham number (Bn) is studied in a wide range of different studied parameters. In this study, isotherms, streamlines and yielded/unyielded zones have been defined. The yielded and unyielded parts have been specified by white and black colors in the contour; respectively. The applied code for the fluid flow and heat transfer is validated by the study of Zhang et al. [14] in the Fig.2 at Ra = 10^5, a = 0.3 L, b = 0.15 L, $x_c = y_c = 0.5$ L, $\theta = 0°$, and Pr = 0.71 for the case of Newtonian fluids in a cooled enclosure with a heated cylinder in the center of the cavity. In addition, the average Nusselt number on the hot circular cylinder is validated between present results and the studies of Zhang et al. [14], Kim et al. [8], and Park et al. [10] in the Table.2 in different Rayleigh numbers. The present approach is applied for isothermal and non-isothermal problems of Bingham fluid recently [35,36] which demonstrates the accuracy of the utilized code for non-Newtonian Bingham fluids properly. An extensive mesh testing procedure was conducted to guarantee a grid independent solution. Six different mesh combinations were explored for the case of Ra= 10^6, (x_c = 0.5 L, y_c = 0.5 L), Ec = 0, Bn = 1, $\theta = 0°$, and a = b = 0.2 L. The average Nusselt numbers on the hot wall have been studied. It was confirmed that the grid size (300*300) ensures a grid independent solution as portrayed by Table 1. In addition, we set the time step $\Delta t = 0.0001$ for this calculation and based on on the validations, the final (developed) stage was defined at the non-dimensional time $t^* = 40$. To see the process of convection and yielding before the final stage, Fig.3 presents the isotherms, streamlines, and yielded/unyielded zone at Ra= 10^6, (x_c = 0.5 L, y_c = 0.5 L), Ec = 0, Bn = 7, $\theta = 0°$, and a = 0.1 L, b = 0.2 L in different non-dimensional time (t^* = 5, 10, 15, 30, and 40). The running time for the grid size (300 * 300) is 5791 seconds. The value of σ was varied in each iteration according to the Appendix.

5 Results and discussion

Fig.4 shows the streamlines, the isotherms, and the yielded/unyielded sections in different Rayleigh numbers at $x_c = y_c = 0.5$ L, Bn = 1, Ec =

0, $\theta = 0°$, and a = b = 0.2 L. At Ra=10^4, the temperature contours are circular around the cylinder which demonstrate the conduction is dominated in the enclosure. As the Rayleigh number increases, the movements of the isotherms between the cold cylinder and hot walls ameliorate significantly and they become progressively curved. Moreover, the gradient of temperature on the hot wall augments with the rise of Rayleigh number. In fact, it occurs while the thermal boundary layer thickness on the side walls decreases with increasing Rayleigh number. The streamlines exhibit that the convection process has been enhanced by the growth of Rayleigh numbers as the core of the streamline changes and the streamlines traverse more distance in the cavity. The last column displays the yielded (White) and unyielded (Black) regions for the studied Rayleigh numbers at Bn = 1. It is clear that the proportion of the unyielded sections in the enclosure has enhanced with the drop of Rayleigh numbers markedly. Therefore, for a constant Bingham number, the increase in Rayleigh number causes the unyielded zones to decline.

Table 3 indicates that the average Nusselt number increases as Rayleigh number rises at Ec = 0, Bn = 1, a = b = 0.2 L, $\theta = 0°$, and ($x_c = y_c$ = 0.5 L). The unyielded sections occupy more spaces in the cavity as the Bingham number augments and the rise of the Bingham number causes the yielded regions to disappear gradually. In other words, there is a critical Bingham number Bn_c above which the fluid is completely unyielded. These numbers are listed in Table 4 for different Rayleigh numbers.

Fig.5 depicts the isotherms in different radii and Bingham numbers at $x_c = y_c = 0.5$ L, Ra = 10^6, Ec = 0, and $\theta = 0°$. In this figure, the isotherms for different ratios of the radii (A = 0.25, 0.5, 1, 2, and 4) have been studied. The figure demonstrates that the convection process of isotherms (The convection process means the movement of the isotherms between the cold cylinder and the hot walls) augments clearly as the ratio of the radius (A) increases. When Bingham number increase, the convection process diminishes gradually. At high Bingham numbers, the isotherms shape into the form of the circular/elliptical. This pattern confirms the conduction process is replaced with convection. As the ratio of radius increases, the pattern to reach the conduction part happens in higher Bingham numbers.

Fig.6 exhibits the streamlines in different radii and Bingham numbers at $x_c = y_c = 0.5$ L, Ra = 10^6, Ec = 0, and $\theta = 0°$. Two symmetric circulation with two vortices are shown in the streamlines in different parameters. The cores of the streamlines become strong as the ratio of the radius increases. It demonstrates that the rise of the ration of radius enhances the convection process. Since the Bingham number increases, the curved shape of the streamline decline and the core of the circulation move from the bottom to center. Finally, the form of the streamline shows that the conduction dominates the flow field and a relatively weak

convective flow can be observed at the higher Bingham number.

Fig.7 displays the yielded/unyielded sections in different radii and Bingham numbers at $x_c = y_c = 0.5$ L, Ra = 10^6, Ec = 0, and $\theta = 0°$. Since, it is concentric annual, the unyielded zons are symmetric for different parts. At Bn = 1, the main unyielded regions appear on the top of the cylinder and the top left and right corners. As the ratio of the radii (A) increases the unyielded zone on the top of the cylinder diminishes and the top corners sections alters. In addition, two curved shapes of unyielded parts in the bottom of the cylinder at A = 0.25 decreases gradually with the rise of the ratio of radii and nearly disappear at A = 2. At Bn = 4, the unyielded zones on the top and bottom of the cylinder as well as the top corners develop in different the ratio of radii. As Bingham number rises from Bn = 4 to 8, the unyielded zone increases significantly At A = 0.25 and 0.5 as the only two small symmetric yielded parts at A = 0.25 was observed around the elliptic cylinder. At A = 1 and 2, two crescent shapes of unyielded sections are generated in addition to the small part on the top of the cylinder; although, these parts are smaller at A = 2 compared to A = 1. Further, two unyielded parts close to the sidewalls appear at A = 1. At A = 4 and Bn = 8, the effect of Bingham number was visible on the top of the cavity close to the sidewall. The increase in Bingham number from Bn = 8 to 10, causes the space between the inner cylinder and the cavity fills utterly with the unyielded materials for A = 0.25. Thus, the critical Bingham number (Bn_c) for A = 0.25 is observed at $Bn_c = 10$. For A = 0.5, there are just two small yielded parts next to the cylinder while other parts are unyielded. At A=1 and 2, the unyielded zones develop; however, this development is more observable at A = 1. For A = 2 and Bn = 10, there is a marginal alteration occurs in the form and size of the unyielded part. It was found, the critical Bingham number of A = 0.5 is at Bn = 12 as the space between cavity and the inner cylinder is filled with the unyielded materials. At A = 1, there are only two narrow crescent yielded parts. In addition, the share of the unyielded sections augment considerably at A = 2 and 4 for Bn = 12. The figure demonstrates that for A = 1, 2 and 4, the critical Bingham numbers were obtained at Bn = 14, 16 and 18; respectively.

Fig.8 shows the local Nusselt numbers on the left wall (Nu_L) and the bottom wall (Nu_b) in different Bingham numbers at $x_c = y_c = 0.5$ L, Ra = 10^6, Ec = 0, $\theta = 0°$, and a = b = 0.2 L. The local Nusselt numbers on the left wall (Nu_L) depicts that Bn = 1 and 4, there is a high peak at Y = 0.2 where this peak value drops considerably from Bn = 1 to 4. In addition, it falls steadily from Y = 0.2 to 1 at Bn = 1 and 4. At higher Bingham numbers (Bn = 8, 10, 12 , and 14), the peak value is observed at Y = 0.5 for the Nu_L as it has a curved shape and in a symmetric form. In addition, it is clear that the difference between values for Nu_L at Bn $\geq$ 0.8 is marginal. The local Nusselt numbers on the bottom wall (Nu_b) at Bn = 1 and 4 has a sinusoidal manner which the pick values are seen

at Y = 0.2 and 0.8. As Bingham number increases from Bn = 4 to 8, the sinusoidal behavior alters to a curved shape and the values of local Nusselt number declines considerably. The rise of the Bingham number from Bn = 8 to 10 causes the local Nusselt number to decline slightly, but the local Nusselt numbers for Bingham numbers of Bn = 10, 12, and 14 are nearly the same.

Fig.9 demonstrates that the average Nusselt numbers on the top wall (Nu_{Tavg}), the left wall (Nu_{Lavg}) and the bottom wall (Nu_{Bavg}) in different Bingham numbers and aspect ratios of the radii at $x_c = y_c = 0.5$ L, Ra = 10^6, Ec = 0, and $\theta = 0°$. It should be noted that the average Nusselt numbers on the right and left walls are the same because of the symmetric shape, so the average Nusselt number of the right wall is not depicted here. The figure shows that Nu_{Bavg} in different ratios of radii drop gradually as the Bingham number increases. Generally, it can be seen that the increase in the ratio of the radii for various Bingham numbers augments Nu_{Bavg}. In contrast with Nu_{Bavg}, Nu_{Lavg} has irregular behaviour against the rise of Bingham number and ratios of radii. However, Nu_{Tavg} from Bn = 1 to 8 enhances steadily in all studied ratios of radii. At A = 1, 2, and 4, the increase in the Nu_{Tavg} continues from Bn = 8 to 16, but at A = 0.25 and 0.5, the Nu_{Tavg} declines from Bn = 8 to 12.

Table 5 presents the total average Nusselt numbers ($Nu_{tot_{avg}}$) in different Bingham numbers and the ratio of radii (A) at Ec = 0, Ra = 10^6, $\theta = 0°$, and ($x_c = y_c = 0.5$ L). It demonstrates that the total average Nusselt number decreases gradually as Bingham number rises for different ratio of radii (A). It shows that the least total average Nusselt numbers are observed at A = 0.25 for different Bingham numbers. But, the highest value among different ratio of radii (A) is different for various Bingham numbers. The highest values are found at A = 2, 4, 1, 1, and 1 for Bingham numbers of Bn = 4, 8, 10, 12 , and 14.

Fig.10 illustrates the isotherms in different sizes and Bingham numbers at $x_c = y_c = 0.5$ L, Ra = 10^6, Ec=0, and $\theta = 0°$. It displays that the rise of the cylinder size augments the convection process between the hot walls and the cylinder. When Bingham number increase, the convection process diminishes gradually in different sizes of the inner cylinder.

Fig.11 demonstrates the streamlines in different sizes and Bingham numbers at $x_c = y_c = 0.5$ L, Ra = 10^6, Ec=0, and $\theta = 0°$. It depicts that the rise of the cylinder size causes the core of the streamline separated into two cores and demonstrates the convection strengthens. However, the rise of Bingham number weakens the streamline where the core of the streamlines move toward the top of the cavity and the streamlines movements drop considerably.

Fig.12 reveals the yielded/unyielded zones in different sizes and Bingham numbers at $x_c = y_c = 0.5$ L, Ra = 10^6, Ec=0, and $\theta = 0°$. At Bn = 1, the top left and right corners of the cavity are occupied with unyielded

sections and some small unyielded parts around the cylinder for a = b = 0.1 L. As the size of the cylinder increases from a = b =0.1 L to 0.2 L, the unyielded parts diminish; especially the top and left corners of the cavity. But, the rise of the cylinder size to a = b = 0.3 L provokes a large unyielded section appears under the cylinder and two symmetric small unyielded sections are generated close to sidewalls. In the following pattern, unyielded regions are generated on the top and bottom of the cavity at a = b = 0.4 L. At Bn = 4, the increase in Bingham number at a = b = 0.1 L results in the occupation of the top of the cavity with uyielded parts and two symmetric large parts around the cylinder. But, the effect of the increase in Bingham number to Bn = 4 is marginal for a = b = 0.2 L compared to a = b = 0.1 L where the unyielded parts develop slightly. For a = b = 0.3 L, the unyielded zone on the bottom of the cylinder develops and an unyielded part is created on the top of the cylinder. The same trend is observed at a = b = 0.4 L where two large unyielded sections on the top and bottom of the cavity are present and two other unyielded next to the cylinder and the sidewalls appear. At Bn = 8, interestingly, for a = b = 0.1 L, the unyielded part on the top of the cavity diminishes; although, unyielded parts in the bottom corners and in the middle of the cavity enlarge considerably. The unyielded zones develop vastly for a = b = 0.2 L, where two new unyielded parts close to the top and sidewalls of the cavity are generated. At a = b = 0.3 L, there are only two symmetric yielded parts between the cylinder and the side walls while other parts are occupied by the unyielded zones. It was found the Bingham number of Bn = 8 is the critical Bingham number for a = b = 0.2 L since the cavity is filled by the unyielded sections. At Bn = 10, there are two small yielded sections between the cold cylinder and the hot walls at a = b = 0.1 L and 0.2 L and other parts filled with unyielded regions. However, it should be noted the share of the unyielded parts are larger at a = b = 0.1 L compared to a = b = 0.2 L. At a = b = 0.3 L, two very narrow crescent yielded parts are present and other sections are unyielded. At Bn = 12, it was observed that the critical Bingham number (Bn_c) for a = b = 0.3 L is at this Bigham number ($Bn_c = 12$). In addition, two small curved shapes of the yielded parts are present at a = b = 0.1 L and 0.2 L while other sections are yielded. Finally, the figure demonstrates that the critical Bingham number for the ratii of a = b = 0.1 and 0.2 L are equal to $Bn_c = 14$.

Table 6 exhibits total average Nusselt numbers in different Bingham numbers and sizes of the inner cylinder at A = 1, Ec = 0, $\theta = 0^\circ$, Ra = 10^6, and ($x_c = y_c = 0.5$ L). It indicates the rise of the cylinder size enhances the total average Nusselt number for different Bingham numbers. In addition, it reveals that the increase in Bingham number declines the total average Nusselt number gradually.

Fig.13 shows the isotherms in different horizontal positions and Bingham numbers at $y_c = 0.5$ L, Ra = 10^6, Ec = 0, and a = b = 0.2 L, and

$\theta = 0°$. It depicts that the movement of the isotherms between the cold inner cylinder and the hot walls augment as the cylinder moves to the side walls of the cavity in different Bingham numbers. It confirms that the convection process augments due to the horizontal movement from the center of the cavity. In addition, the rise of the Bingham number diminishes the movement of the isotherms between the cylinder and the enclosure walls clearly which proves the drop of the convection of heat transfer.

Fig.14 depicts the streamlines in different horizontal positions and Bingham numbers at y_c = 0.5 L, Ra = 10^6, Ec = 0, and a = b = 0.2 L, and $\theta = 0°$. It shows that the horizontal change in the location of the cylinder from the concentric to eccentric positions causes the two symmetric streamlines convert to main large and secondary small vortexes. This pattern causes the convection to augment considerably. The rise of Bingham number weakens the streamlines and at high Bingham number of Bn = 14 third small vortex on the top left of the cavity is generated.

Fig.15 illustrates the yielded/unyielded sections in different horizontal positions and Bingham numbers at y_c = 0.5 L, Ra = 10^6, Ec = 0, and a = b = 0.2 L, and $\theta = 0°$. At Bn = 1, as the cylinder moves from the center of the cavity to the side walls horizontally, unyielded zones on the top corners; especially; the corners close to the cylinder enlarge significantly. In addition, the unyielded part on the top of the cylinder also expands slightly. At Bn = 4, the movement of the cylinder from center to the side walls unyielded zones; significantly, expand on the top left and right corners and the bottom corner close to the cylinder. Moreover, the unyielded part of the top of the cylinder changes from a small position to a large part. For Bn = 8, at the space between the cylinder and the side wall close to the eccentric cylinders, the unyielded parts fill the sections next to the side wall; especially, the corners of the cavity in this side. At Bn = 10 and 12, the pattern continues where the space between the cold and the side wall for the eccentric position fills with the unyielded part while the yielded parts are present in another side of the cylinder. In addition, at Bn = 12, it is clear that for the concentric cylinder, the unyielded parts have occupied the most parts of the cavity and just there are two narrow curved yielded materials around the cylinder. It demonstrates that for the center positioned cylinder, the critical Bingham number is at Bn = 14 while eccentric cylinders have still small yielded parts around the cylinder. Finally, it was found that the cavity fills with the unyielded material for the both eccentric cases at Bn = 18.

Table 7 indicates total average Nusselt numbers in different Bingham numbers and horizontal positions (x_c) at Ec = 0, $\theta = 0°$, Ra = 10^6, a= b = 0.2 L, and y_c = 0.5 L. It confirms that the total average Nusselt number increases in different Bingham numbers as the cylinders move from the center toward side walls horizontally. In addition, for different horizontal positions, the increase in Bingham number declines the total

average Nusselt number gradually.

Fig.16 shows the isotherms in different vertical positions and Bingham numbers at $x_c = 0.5$ L, Ra $= 10^6$, Ec $= 0$, and a $=$ b $= 0.2$ L, and $\theta = 0°$. At Bn $= 1$, it displays that the movement of the cylinder from the bottom of the cavity to the top side increases the development of the isotherms in the cavity. It confirms that the convection process strengthens with the movement of the cylinder from the top to the bottom side of the cavity vertically. Further, the rise of Bingham number declines the convection process for different vertical positions. But, at Bn $= 8$ and 14, the lowest convection process of the isotherms are observed for the concentric case.

Fig.17 exposes the streamlines in different vertical positions and Bingham numbers at $x_c = 0.5$ L, Ra $= 10^6$, Ec $= 0$, and a $=$ b $= 0.2$ L, and $\theta = 0°$. It shows that the location of the cylinder moves toward the top of the cavity causes the the core of the streamlines of two symmetric streamlines to become weak which demonstrates the convection process weakens significantly. In addition, the rise of Bingham number weakens the streamlines for different vertical positions.

Fig.18 displays the yielded/unyielded zones in different vertical positions and Bingham numbers at $x_c = 0.5$ L, Ra $= 10^6$, Ec $= 0$, and a $=$ b $= 0.2$ L, and $\theta = 0°$. At Bn $= 1$, as the cylinder is close to the bottom wall ($y_c = 0.3$ L), the unyielded section is generated next to the top wall considerably and also the unyielded parts are formed under the cylinder and there is a small unyielded part on the top of the cylinder. As the cylinder moves from $y_c = 0.3$ L to 0.5 L and 0.7 L,the large unyielded parts close to the top and bottom horizontal walls of the cylinder disappears and the unyielded zone diminishes significantly. At Bn $= 4$, at $y_c =$ 0.3 L, the unyielded parts on the top and bottom of the cavity expands and some other small unyielded parts are generated. At $y_c = 0.5$ L, the unyielded parts decline significantly and just small unyielded parts on the top corners of the cavity and around the cylinder are present. At x_c $= 0.7$ L, the the most dense unyielded part is observed between the inner cylinder and the top side cavity and there are narrow unyielded parts on the top corners of the cavity. At Bn $= 8$, for $y_c = 0.3$ L, nearly the top half of the cavity is filled with unyielded parts while the symmetric unyielded parts next to the cylinder and the side walls are created at this Bingham number. Further, the unyielded part under the cylinder is nearly the same as Bn $= 4$. For $y_c = 0.5$ L, the unyielded parts are developed on the top of the cylinder, the side walls, and next to the cylinder. For $y_c = 0.7$ L, a narrow unyielded part covers the bottom side of the cavity while the unyielded part on the top of the cylinder is extended. Moreover, the unyielded parts on the bottom of the cylinder and side walls strengthens considerably. At Bn $= 10$, it demonstrates that the unyielded parts cover the most parts of the cavity for the positions of $y_c =$ 0.3 L and 0.7 L and there is only small curved yielded parts around the cylinder. But, for the concentric case the yielded parts are more than the

eccentric cases. This pattern is also observed at Bn = 12 where there are symmetric arrow crescent yielded parts around the cylinder. Finally, at Bn = 14, the space between cavity and the inner cylinder is filled with the unyielded materials.

Table 8 cites total average Nusselt numbers in different Bingham numbers and vertical positions (y_c) at $\theta = 0°$, Ec = 0, Ra = 10^6, a= b = 0.2 L, and x_c = 0.5 L. It demonstrates that at Bn = 1 and 4, the total average Nusselt number declines gradually as the cylinder moves from y_c = 0.3 L to 0.7 L. But, for other Bingham numbers, the maximum total average Nusselt numbers among different vertical positions are obtained at the position of y_c = 0.3 L while the least values were observed for the concentric case (y_c = 0.5 L). Moreover, it indicates that the increase in Bingham number declines the total average Nusselt number regularly in various vertical positions.

Fig.19 portrays the isotherms in different inclined angles and Bingham numbers at $x_c = y_c$ = 0.5 L, Ra = 10^6, Ec = 0, and a = b = 0.2 L. When the inclined angles increase, the buoyancy force divide into vertical and horizontal forces throughout the cavity. Therefore, the shapes of the isotherms change and the alteration provokes the heat transfer process in the cavity to ameliorate or reduce. The rise of Bingham number enhances the gradient of isotherms on the cylinder and the movements of the isotherms between the cylinder and the hot walls diminish substantially. Therefore, heat transfer declines considerably as Bingham number increases in various inclined angles.

Fig.20 demonstrates the streamlines in different inclined angles and Bingham numbers at $x_c = y_c$ = 0.5 L, Ra = 10^6, Ec = 0, and a = b = 0.2 L. The inclined angle causes the buoyancy forces applies to different directions and not only in the vertical direction. So, the circulation and values of the two symmetric streamlines around the cylinder alter. This alteration confirms that the convection process changes due to the inclined angle. As Bingham number increases, the streamlines weaken evidently and therefore convection process drops.

Fig.21 depicts the yielded/unyielded sections in different inclined angles (θ) and Bingham numbers (Bn) at $x_c = y_c$ = 0.5 L, Ra = 10^6, Ec = 0, and a = b = 0.2 L. At Bn = 1 and 4, the unyielded part expands on the top corner of the cavity at $\theta = 40°$ and 120 while the sizes of unyielded zones do not alter significantly at $\theta = 80°$ compared to $\theta = 0°$. For Bn = 8, the increase in the inclined angles from $\theta = 0°$ to $\theta = 40°$ and 120° causes two unyielded parts on the bottom and top corners of the cavity are generated. But, at $\theta = 80°$, the unyielded zone diminishes slightly compared to $\theta = 0°$. For Bn = 10, interestingly, the most unyielded parts are observed at $\theta = 80°$ in contrast with the previous trends of smaller Bingham numbers. At Bn = 12, there is only a narrow crescent yielded part around the cylinder and other sections are unyielded. Finally, it demonstrates Bn = 14 is the critical Bingham number for different in-

clined angles.

Table 9 states total average Nusselt numbers in different Bingham numbers and inclined angles (θ) at Ec = 0, Ra = 10^6, a= b = 0.2 L, and x_c = y_c = 0.5 L. For Bn = 1, the total average Nusselt number increases considerably as the inclined angle increases from $\theta = 0^\circ$ to 40°, but it drops from $\theta = 40^\circ$ to 80°. The total average Nusselt number enhances again with rise of the inclined angle from $\theta = 80^\circ$ to 120°. At Bn = 4, the maximum and minimum average Nusselt numbers are obtained at inclined angles of $\theta = 0^\circ$ and 40°; respectively. In contrast with the Bingham number of Bn = 4, it shows that for Bn = 8 and 10, the highest and least values of average Nusselt numbers are observed at inclined angles of $\theta = 40^\circ$ and 0°; respectively. At Bn = 12 and 14, the total average Nusselt numbers are nearly the same.

Fig.22 exhibits the isotherms, streamlines and yielded/unyielded parts in different Eckert numbers at x_c = y_c = 0.5 L, Bn = 8, and a = b = 0.2 L, and $\theta = 0^\circ$. It demonstrates that the increase in Eckert number causes the isotherms, streamlines and the unielded/yielded sections to alter slightly.

Table 10 mentions total average Nusselt numbers in different Eckert numbers at Bn = 8, Ec=0, Ra = 10^6, a= b = 0.2 L, $\theta = 0^\circ$, and x_c = y_c = 0.5 L. It shows the total average Nusselt number increases slightly as the Eckert number increases.

6 Concluding Remarks

Natural convection of viscoplastic fluids in an inclined heated enclosure with an inner cold cylinder in the presence of viscous dissipation has been analyzed by Lattice Boltzmann method (LBM). In this study, the Bingham model without any regularization has been studied for the simulation of viscoplastic fluids. Fluid flow, heat transfer, and yielded/unyielded have been conducted for certain pertinent parameters of Rayleigh number (Ra = 10^4, 10^5 and 10^6), Bingham number (Bn = 1 - Bn_c), Eckert number (Ec = 0.01, 0.1, and 1), the size of the inner cylinder, various inclined angles of the cavity ($\theta = 0^\circ$, 40°, 80°, 120°), the ratio of radii of the inner cylinder (A = 0.25, 0.5, 1, 2, and 4), and different positions of the inner cylinder. The main conclusions of the present investigation can be summarized as follows:

- Heat transfer enhances with augmentation of Rayleigh number in different studied parameters.
- The average Nusselt numbers demonstrate that the heat transfer declines with the rise of the Bingham number in various studied parameters.
- It was found that the rise of Bingham number augments the unyielded part, but provokes the heat transfer to drop gradually.

- The enhancement of Rayleigh number increases the critical Bingham number significantly.
- The increase in the ratio of the cylinder radii (A = b/a) for the concentric case ($x_c = y_c = 0.5$) enhance heat transfer.
- The unyielded zones diminish gradually as the ratio of the cylinder radii (A = b/a) for the concentric case ($x_c = y_c = 0.5$) increases.
- The rise of the cylinder size for the concentric case ($x_c = y_c = 0.5$) augment heat transfer and the unyielded zone.
- The movement of the cylinder from the center of the cavity to side walls horizontally augments heat transfer while the unyielded parts decrease and the critical Bingham number rises.
- The movement of the cylinder from the bottom of the cavity to top side wall of the cavity vertically drops heat transfer while the unyielded parts enlarge and the critical Bingham number declines.
- The alteration of inclined angle changes heat transfer and the unyielded zones significantly.
- The rise of Eckert number rises the average Nusselt number slightly, and changes the unyielded regions insignificantly. Therefore, in this problem, we can assume the viscous dissipation term is negligible.

Acknowledgements

The first author(Gholamreza Kefayati (GH. R. Kefayati)) gratefully acknowledges the funding support in the form of a Research Fellowship awarded him by the Hong Kong Polytechnic University.

Appendix

Here, we shall discuss the stability of the numerical scheme. Finding the parameter σ, we multiply f_α^{eq} with $|\boldsymbol{\xi}_\alpha|^2/2$ and take the sum, which leads to

$$\sum_{\alpha=0}^{8} \frac{1}{2} f_\alpha^{eq} |\boldsymbol{\xi}_\alpha|^2 = p + \frac{1}{2}\rho \left|\mathbf{u}\right|^2 - \frac{\tau_{xx}+\tau_{yy}}{2}. \tag{A1}$$

Next, it is easy to verify that

$$\sum_{\alpha=0}^{8} F_\alpha |\boldsymbol{\xi}_\alpha|^2 = 0. \tag{A2}$$

Hence,

$$\frac{\partial}{\partial t}\left[p + \frac{1}{2}\rho|\mathbf{u}|^2 - \frac{\tau_{xx}+\tau_{yy}}{2}\right] + \frac{\sigma^2}{2}\rho(\nabla\cdot\mathbf{u}) = O\left(\varepsilon\right). \tag{A3}$$

The Courant-Friedrichs-Lewy (CFL) condition states that [57,58]

$$K = \frac{u\Delta t}{\Delta x} + \frac{v\Delta t}{\Delta y} \leq 1. \tag{A4}$$

This can be used in (A3) and we obtain

$$\left[\left|\mathbf{u}\right|^2 + \frac{2p - \tau_{xx} - \tau_{yy}}{\rho}\right] + \sigma^2 K = O\left(\varepsilon\right). \tag{A5}$$

Thus, the lattice speed σ must satisfy

$$\sigma = K_c\sqrt{\left|\frac{\tau_{xx}+\tau_{yy}-2p}{\rho} - \left|\mathbf{u}\right|^2\right|}, \quad K_c = \frac{1}{\sqrt{K}} \geq 1. \tag{A6}$$

Since the pressure p has to be uniquely defined in a Bingham fluid, one requires that $\tau_{xx}+\tau_{yy}=0$;. Thus, reduces to

$$\sigma = K_c\sqrt{\left|\frac{-2p}{\rho} - \left|\mathbf{u}\right|^2\right|}, \quad K_c = \frac{1}{\sqrt{K}} \geq 1 \tag{A7}$$

As a result, the value σ is modified and changes in each iteration as defined through (A7).

References

[1] D. Vola, L. Boscardin, J. Latche, Laminar unsteady flows of Bingham fluids: a numerical strategy and some benchmark results. J. Comput. Phys., 187 (2003) 441-456.

[2] Osman Turan, Nilanjan Chakraborty, Robert J. Poole, Laminar natural convection of Bingham fluids in a square enclosure with differentially heated side walls, J. Non-Newtonian Fluid Mech. 165 (2010) 901-913.

[3] Osman Turan, Robert J. Poole, Nilanjan Chakraborty, Aspect ratio effects in laminar natural convection of Bingham fluids in rectangular enclosures with differentially heated side walls. J. Non-Newt. Fluid Mech., 166 (2011) 208-230.

[4] Osman Turan, Nilanjan Chakraborty, Robert J. Poole, Laminar Rayleigh-Bnard convection of yield stress fluids in a square enclosure. J. Non-Newt. Fluid Mech., 171-172 (2012) 83-96.

[5] R.R. Huilgol, G.H.R. Kefayati, Natural convection problem in a Bingham fluid using the operator-splitting method, Journal of Non-Newtonian Fluid Mechanics 220 (2015) 22-32.

[6] I. Karimfazli, I. A. Frigaard, A. Wachs, A novel heat transfer switch using the yield stress, Journal of Fluid Mechanics 783 (2015) 526-566.

[7] C. Shu, H. Xue, Y.D. Zhu, Numerical study of natural convection in an eccentric annulus between a square outer cylinder and circular inner cylinder using DQ method, Int. J. Heat Mass Transfer 44 (2001) 3321-3333.

[8] B.S. Kim, D.S. Lee, M.Y. Ha, H.S. Yoon, A numerical study of natural convection in a square enclosure with a circular cylinder at different vertical locations, International Journal of Heat and Mass Transfer 51 (2008) 1888-1906.

[9] A. A. Mehrizi, K. Sedighi, M. Farhadi, M. Sheikholeslami, Lattice Boltzmann simulation of natural convection heat transfer in an elliptical-triangular annulus, International Communications in Heat and Mass Transfer 48 (2013) 164-177.

[10] Yong Gap Park, Man Yeong Ha, Changyoung Choi, Jaehyun Park, Natural convection in a square enclosure with two inner circular cylinders positioned at different vertical locations, International Journal of Heat and Mass Transfer 77 (2014) 501-518.

[11] A. A. Mehrizi, A. A. Mohamad, Effect of the inclination angle and eccentricity on free Convection heat transfer in ellipticaltriangular annuli: A Lattice Boltzmann approach, Numerical Heat Transfer, Part A: Applications 68 (2015) 17-43.

[12] Gi Su Mun, Jeong Hoon Doo, Man Yeong Ha, Thermo-dynamic irreversibility induced by natural convection in square enclosure with inner cylinder. Part-I: Effect of tilted angle of enclosure, International Journal of Heat and Mass Transfer 97 (2016) 1102-1119.

[13] Gi Su Mun, Yong Gap Park, Hyun Sik Yoon, Minsung Kim, Man Yeong Ha, Natural convection in a cold enclosure with four hot inner cylinders

based on diamond arrays (Part-I: Effect of horizontal and vertical equal distance of inner cylinders), International Journal of Heat and Mass Transfer 111 (2017) 755-770.

[14] Ping Zhang, Xiaohua Zhang, Jiheng Deng, Laizhong Song, A numerical study of natural convection in an inclined square enclosure with an elliptic cylinder using variational multiscale element free Galerkin method, International Journal of Heat and Mass Transfer 99 (2016) 721-737.

[15] A. K. Baranwal, R. P. Chhabra, Effect of fluid Yield stress on natural convection from horizontal cylinders in a square enclosure, Heat Transfer Engineering 38 (2017) 557-577.

[16] Ashin Dutta , Anoop K. Gupta , Garima Mishra , R.P. Chhabra, Effect of uid yield stress and of angle of tilt on natural convection from a square bar in a square annulus, Computers and Fluids 160 (2018) 138-163.

[17] A. A. Mohamad, A. Kuzmin, A critical evaluation of force term in lattice Boltzmann method, natural convection problem, International Journal of Heat and Mass Transfer, 53 (2010) 990–996.

[18] H. Nemati, M. Farhadi, K. Sedighi, E. Fattahi, A.A.R. Darzi, Lattice Boltzmann simulation of nanofluid in lid-driven cavity, International Communications in Heat and Mass Transfer 37 (2010) 1528-1534.

[19] A. A. Mehrizi, M. Farhadi, S. Shayamehr, Natural convection flow of Cu-Water nanofluid in horizontal cylindrical annuli with inner triangular cylinder using lattice Boltzmann method, International Communications in Heat and Mass Transfer 44 (2013) 147-156.

[20] H. R. Ashorynejad, A. A. Mohamad, M. Sheikholeslami, Magnetic field effects on natural convection flow of a nanofluid in a horizontal cylindrical annulus using Lattice Boltzmann method, Int. J. Therm. Sci. 64 (2013) 240-250.

[21] A. Abouei Mehrizi, M. Farhadi, H. Hassanzade Afroozi, S. Shayamehr, Lattice Boltzmann simulation of natural convection flow around a horizontal cylinder located beneath an insulation plate J. Theor. Appl. Mech., 51 (2013) 729–739.

[22] A. A. Mehrizi, M. Farhadi, K. Sedighi, M. A. Delavar, Effect of fin position and porosity on heat transfer improvement in a plate porous media heat exchanger J. Taiwan Inst. Chem. Eng., 44 (2013) 420–431.

[23] H. Sajjadi, M. Salmanzadeh, G. Ahmadi, S. Jafari, Turbulent indoor airflow simulation using hybrid LES/RANS model utilizing Lattice Boltzmann method, Computers and Fluids 150 (2017) 66-73.

[24] Dongxing Song, Mohammad Hatami, Jiandong Zhou, and Dengwei Jing, Dynamic Nanoparticle Aggregation for a Flowing Colloidal Suspension with Nonuniform Temperature Field Studied by a Coupled LBM and PBE Method, Ind. Eng. Chem. Res., 56 (2017) 10886-10899.

[25] H. Sajjadi, M. Salmanzadeh, G. Ahmadi, S. Jafari, Simulations of indoor airflow and particle dispersion and deposition by the lattice Boltzmann method using LES and RANS approaches, Building and Environment 102 (2016) 1–12.

[26] H. Sajjadi, M. Gorji, GH. R. Kefayati, D. D. Ganji, Lattice Boltzmann simulation of natural convection in an inclined heated cavity partially using Cu/water nanofluid, International Journal of Fluid Mechanics Research 39 (2012) 348–372.

[27] H. Sajjadi, GH. R. Kefayati, Lattice Boltzmann simulation of turbulent natural convection in tall enclosures, Thermal Science 19 (2015) 155–166.

[28] H. Sajjadi, GH. R. Kefayati, MHD Turbulent and Laminar Natural Convection in a Square Cavity utilizing Lattice Boltzmann Method, Heat Transfer–Asian Research 45 (2016) 795–814.

[29] S.C. Fu, R.M.C. So, W.W.F. Leung, Linearized-Boltzmann-type-equation based finite difference method for thermal incompressible flow, Computers and Fluids 69 (2012) 67–80.

[30] R.R. Huilgol, GH.R. Kefayati, From mesoscopic models to continuum mechanics: Newtonian and non-newtonian fluids, Journal of Non-Newtonian Fluid Mechanics 233 (2016) 146-154.

[31] R.R. Huilgol, GH.R. Kefayati, A particle distribution function approach to the equations of continuum mechanics in Cartesian, cylindrical and spherical coordinates: Newtonian and non-Newtonian uids, Journal of Non-Newtonian Fluid Mechanics 251 (2018) 146–154.

[32] GH. R. Kefayati, FDLBM simulation of entropy generation in double diffusive natural convection of power-law fluids in an enclosure with Soret and Dufour effects, International Journal of Heat and Mass Transfer 89 (2015) 267–290.

[33] GH. R. Kefayati, Simulation of double diffusive natural convection and entropy generation of power-law fluids in an inclined porous cavity with Soret and Dufour effects (Part I: Study of fluid flow, heat and mass transfer), International Journal of Heat and Mass Transfer 94 (2016) 539–581.

[34] GH. R. Kefayati, Simulation of double diffusive natural convection and entropy generation of power-law fluids in an inclined porous cavity with Soret and Dufour effects (Part II: Entropy generation) , International Journal of Heat and Mass Transfer 94 (2016) 582–624.

[35] GH. R. Kefayati, R.R. Huilgol, Lattice Boltzmann method for the simulation of the steady flow of a Bingham fluid in a pipe of square cross-section, European Journal of Mechanics /B Fluids 65 (2017) 412-422.

[36] GH. R. Kefayati, R.R. Huilgol, Lattice Boltzmann Method for simulation of mixed convection of a Bingham fluid in a lid-driven cavity, International Journal of Heat and Mass Transfer 103 (2016) 725-743.

[37] GH. R. Kefayati, Double-diffusive natural convection and entropy generation of Bingham fluid in an inclined cavity, International Journal of Heat and Mass Transfer 116 (2018) 762–812.

[38] GH. R. Kefayati, H. Tang, simulation of double-diffusive natural convection and entropy generation of Bingham fluid in an open cavity, European Journal of Mechanics / B Fluids (In Press).

[39] GH. R. Kefayati, H. Tang, Double-diffusive natural convection and entropy generation of Carreau fluid in a heated enclosure with an inner circular cold cylinder (Part I: Heat and mass transfer), International Journal of Heat and Mass Transfer 120 (2018) 731–750.

[40] GH. R. Kefayati, H. Tang, Double-diffusive natural convection and entropy generation of Carreau fluid in a heated enclosure with an inner circular cold cylinder (Part II: Entropy generation) , International Journal of Heat and Mass Transfer 120 (2018) 683–713.

[41] Jiandong Zhou, M. Hatami, Dongxing Song, Dengwei Jing, Design of microchannel heat sink with wavy channel and its time-efficient optimization with combined RSM and FVM methods, International Journal of Heat and Mass Transfer 103 (2016) 715–724.

[42] W. Tang, M. Hatami, J. Zhou, D. Jing, Natural convection heat transfer in a nanofluid-filled cavity with double sinusoidal wavy walls of various phase deviations, International Journal of Heat and Mass Transfer 115 (2017) 430–440.

[43] D. Song, M. Hatami, Y. Wang, D. Jing, Y. Yang, Prediction of hydrodynamic and optical properties of TiO2/water suspension considering particle size distribution, International Journal of Heat and Mass Transfer, 92 (2016) 864–876.

[44] M. Hatami, D. Song, D. Jing, Optimization of a circular-wavy cavity filled by nanofluid under the natural convection heat transfer condition, International Journal of Heat and Mass Transfer 98 (2016) 758–767.

[45] M. Hatami, migration around the heated cylinder during the RSM optimization of a wavy-wall enclosure, Advanced Powder Technology 28 (2017) 890–899.

[46] E. C. Bingham, Fluidity and plasticity, McGraw-Hill, New York (1922).

[47] T.C. Papanastasiou, Flow of materials with yield, J. Rheol. 31 (1987) 385-404.

[48] M. Bercovier, M. Engelman, A finite-element method for incompressible non-Newtonian flows, J. Comput. Phys., 36 (1980) 313-326.

[49] E.J. ODonovan, R.I. Tanner, Numerical study of the Bingham squeeze film problem, J. Non-Newt. Fluid Mech. 15 (1984) 75–83.

[50] G. Duvaut, J.L. Lions, Transfert de chaleur dans un fluide de Bingham dont la viscosit dpend de la temprature, J. Funct. Anal. 11 (1972) 93-110.

[51] R. Glowinski, Finite element methods for incompressible viscous flow, Handbook of Numerical Analysis, vol. 9, 2003, 31176.

[52] P.L. Quere, T.A. de Roquefort, Computation of natural convection in two dimensional cavities with Chebyshev polynomials, J. Comput. Phys. 57 (1985) 210–228.

[53] E. F. Toro, Riemann Solvers and Numerical Methods for Fluid Dynamics: A Practical Introduction. Springer, 1999, pp. 531–542.

[54] P. D. Lax, B. Wendroff, Systems of conservation laws, Comm. Pure Appl. Math. 13 (1960) 217–237.

[55] Q. Zou, X. He, On pressure and velocity boundary conditions for the lattice Boltzmann BGK model. Phys. Fluids, 9 (1997) 1591–1598.

[56] Z. Guo, B. Shi, C. Zheng, A coupled lattice BGK model for the Boussinesq equations. Int. J. Numer. Methods Fluids, 39 (2002) 325–342.

[57] J. Blazek, (2001) Computational Fluid Dynamics: Principles and Applications. Elsevier, 347–350.

[58] T. Cebeci, J. P. Shao, F. Kafyeke, E. Laurendeau, (2005) Computational Fluid Dynamics for Engineers. Springer, 311–320.

Nomenclature

$\mathbf{A}$ The first Rivlin-Ericksen tensor
A The ratio of the inner cylinder radii
a Horizontal radius
Bn Bingham number
b Vertical radius
c Lattice speed
c_p Specific heat capacity at constant pressure
Ec Eckert number
F External forces
f_α Density distribution functions for the specific node of α
f_α^{eq} Equilibrium density distribution functions for the specific node of α
g_α Internal energy distribution functions for the specific node of α
g_α^{eq} Equilibrium internal energy distribution functions for the specific node of α
g Gravity
k Thermal conductivity
L Length of the cavity
$\mathbf{N}$ Body force
Nu Nusselt number
p Pressure
Pr Prandtl number
Ra Rayleigh number
T Temperature
t Time
x, y Cartesian coordinates
x_c, y_c The horizontal and vertical positions of the cylinder center
u Velocity in x direction
U The buoyancy velocity scale
v Velocity in y direction

Greek letters

β_T Thermal expansion coefficient
ϕ Relaxation time
$\boldsymbol{\tau}$ Shear stress
τ_y Yield stress
ξ Discrete particle speeds
Δx Lattice spacing in x direction
Δy Lattice spacing in y direction
Δt Time increment
α Thermal diffusivity
ρ Density of fluid

$\mathbf{\Lambda}$ The viscoplasticity constraint
θ The inclined angle of the cavity

Subscripts

avg Average
B Bottom
C Cold
c Center of the cylinder
d Dynamic
H Hot
L Left
x, y Cartesian coordinates
α Specific node
R Right
s Static
T Top
tot Total

Table 1
Grid independence study at Ra = 10^6, Bn = 1, Ec = 0, a = b = 0.2 L, $\theta = 0°$, x_c = y_c = 0.5 L

Mesh size	$Nu_{tot_{avg}}$
100*100	10.0413
150*150	9.8372
200*200	9.2509
250*250	9.1081
300*300	8.9605
350*350	8.9605

Table 2
Comparison of the average Nusselt number on the hot circular cylinder (a = b = 0.2 L) between the present result and previous studies for Newtonian fluids (Bn = 0) in different Rayleigh numbers at $\theta = 0°$, and ($x_c = y_c = 0.5$ L)

	Present study	Zhang et al. [14]	Kim et al. [8]	Park et al. [10]
Ra = 10^3	5.105	5.103	5.093	5.107
Ra = 10^4	5.116	5.087	5.108	5.128
Ra = 10^5	7.791	7.651	7.767	7.836
Ra = 10^6	14.201	14.024	14.110	14.462

Table 3
Total average Nusselt numbers in different Rayleigh numbers at Ec = 0, Bn = 1, a = b = 0.2 L, $\theta = 0^{\circ}$, and ($x_c = y_c = 0.5$ L)

	Ra = 10^4	Ra = 10^5	Ra = 10^6
$Nu_{tot_{avg}}$	6.2506	7.0525	8.9606

Table 4
The critical Bingham number in different Rayleigh numbers at Ec = 0, Bn = 1, a = b = 0.2 L, $\theta = 0^{\circ}$, and ($x_c = y_c = 0.5$ L)

	Ra = 10^4	Ra = 10^5	Ra = 10^6
Bn_c	1.75	4.5	14

Table 5
Total average Nusselt numbers in different Bingham numbers and the ratio of radii (A) at Ec = 0, Ra = 10^6, $\theta = 0°$, and ($x_c = y_c = 0.5$ L)

	Bn = 1	Bn = 4	Bn = 8	Bn = 10	Bn = 12	Bn = 14	Bn = 16
A = 0.25	3.819	0.943	0.869	0.868	0.870	-	-
A = 0.5	6.017	2.098	1.294	1.293	1.298	-	-
A = 1	8.961	6.435	2.859	2.657	2.642	2.639	-
A = 2	8.991	8.176	3.490	1.755	1.342	1.299	1.296
A = 4	8.869	8.419	5.047	2.144	1.044	0.888	0.875

Table 6
Total average Nusselt numbers in different Bingham numbers and sizes of the inner cylinder at A = 1, Ec = 0, $\theta = 0^\circ$, Ra = 10^6, and ($x_c = y_c = 0.5$ L)

	Bn = 1	Bn = 4	Bn = 8	Bn = 10	Bn = 12	Bn = 14
a = b =0.1 L						
$Nu_{tot_{avg}}$	6.623	4.368	0.581	0.533	0.531	0.529
a = b = 0.2 L						
$Nu_{tot_{avg}}$	8.961	6.435	2.859	2.657	2.642	2.639
a = b = 0.3 L						
$Nu_{tot_{avg}}$	13.098	10.637	8.504	8.445	8.444	-
a = b = 0.4 L						
$Nu_{tot_{avg}}$	22.025	20.710	20.450	20.448	20.450	-

Table 7
Total average Nusselt numbers in different Bingham numbers and horizontal positions (x_c) at Ec = 0, $\theta = 0°$, Ra = 10^6, a= b = 0.2 L, and y_c = 0.5 L

	Bn = 1	Bn = 4	Bn = 8	Bn = 10	Bn = 12	Bn = 14	Bn = 16
$x_c = 0.3$ L							
$Nu_{tot_{avg}}$	9.524	7.684	5.786	5.264	5.128	5.1074	5.1072
$x_c = 0.5$ L							
$Nu_{tot_{avg}}$	8.961	6.435	2.859	2.657	2.642	2.639	-
$x_c = 0.7$ L							
$Nu_{tot_{avg}}$	9.522	7.675	5.770	5.264	5.129	5.1096	5.1094

Table 8
Total average Nusselt numbers in different Bingham numbers and vertical positions (y_c) at $\theta = 0°$, Ec = 0, Ra = 10^6, a= b = 0.2 L, and x_c = 0.5 L

	Bn=1	Bn=4	Bn=8	Bn=10	Bn=12	Bn=14
y_c = 0.3 L						
$Nu_{tot_{avg}}$	11.247	9.778	6.207	5.280	5.168	5.159
y_c = 0.5 L						
$Nu_{tot_{avg}}$	8.961	6.435	2.859	2.657	2.642	2.639
y_c = 0.7 L						
$Nu_{tot_{avg}}$	6.779	4.063	4.365	4.931	5.040	5.052

Table 9
Total average Nusselt numbers in different Bingham numbers and inclined angles (θ) at Ec = 0, Ra = 10^6, a= b = 0.2 L, and $x_c = y_c = 0.5$ L

	Bn = 1	Bn = 4	Bn = 8	Bn = 10	Bn = 12	Bn = 14
$\theta = 0°$						
$Nu_{tot_{avg}}$	8.961	6.435	2.859	2.657	2.642	2.639
$\theta = 40°$						
$Nu_{tot_{avg}}$	10.489	5.802	3.067	2.697	2.645	2.645
$\theta = 80°$						
$Nu_{tot_{avg}}$	9.111	6.762	2.876	2.656	2.644	2.642
$\theta = 120°$						
$Nu_{tot_{avg}}$	10.180	5.820	3.013	2.682	2.644	2.639

Table 10
Total average Nusselt numbers in different Eckert numbers at Bn = 8, Ec=0, Ra = 10^6, a= b = 0.2 L, $\theta = 0°$, and $x_c = y_c = 0.5$ L

	Ec = 0	Ec = 0.01	Ec = 0.1	Ec = 1
$Nu_{tot_{avg}}$	2.859	2.861	2.874	2.915

List of Figures

= 0.2 L, and $\theta = 0^\circ$

Fig.14 The comparison of the streamlines in different horizontal positions and Bingham numbers at y_c = 0.5 L, Ra = 10^6, Ec = 0, and a = b = 0.2 L, and $\theta = 0^\circ$

Fig.15 The comparison of the yielded/unyielded zones in different horizontal positions and Bingham numbers at y_c = 0.5 L, Ra = 10^6, Ec=0, and a = b = 0.2 L, and $\theta = 0^\circ$

Fig.16 The comparison of the isotherms in different vertical positions and Bingham numbers at x_c = 0.5 L, Ra = 10^6, Ec=0, and a = b = 0.2 L, and $\theta = 0^\circ$

Fig.17 The comparison of the streamlines in different vertical positions and Bingham numbers at x_c = 0.5 L, Ra = 10^6, Ec = 0, and a = b = 0.2 L, and $\theta = 0^\circ$

Fig.18 The comparison of the yielded/unyielded zones in different vertical positions and Bingham numbers at x_c = 0.5 L, Ra = 10^6, Ec=0, and a = b = 0.2 L, and $\theta = 0^\circ$

Fig.19 The comparison of the isotherms in different inclined angles and Bingham numbers at $x_c = y_c$ = 0.5 L, Ra = 10^6, Ec = 0, and a = b = 0.2 L

Fig.20 The comparison of the streamlines in different inclined angles and Bingham numbers at $x_c = y_c$ = 0.5 L, Ra = 10^6, Ec = 0, and a = b = 0.2 L

Fig.21 The comparison of the yielded/unyielded zones in different inclined angles and Bingham numbers at $x_c = y_c$ = 0.5 L, Ra = 10^6, Ec = 0, and a = b = 0.2 L

Fig.22 The comparison of the isotherms, streamlines and yielded/unyielded parts in different Eckert numbers (Ec = 0 (red line) and Ec = 1 (dashed green line)) at $x_c = y_c$ = 0.5 L, Bn = 8, and a = b = 0.2 L, and $\theta = 0^\circ$

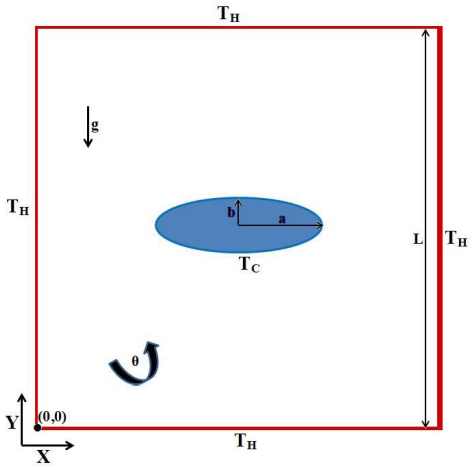

Fig. 1. The geometry of the present problem

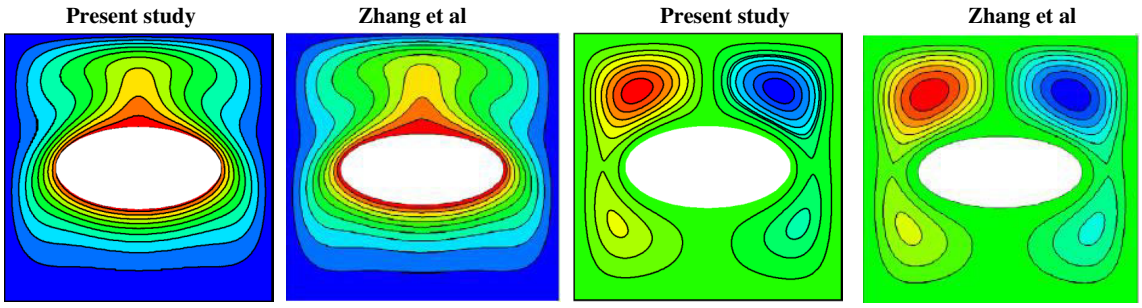

Fig. 2. The comparison of the isotherms and streamlines between present study and Zhang et al. [14] at Ra = 10^5, a = 0.3 L, b = 0.15 L, $x_c = y_c = 0.5$ L, $\theta = 0°$, and Pr = 0.71

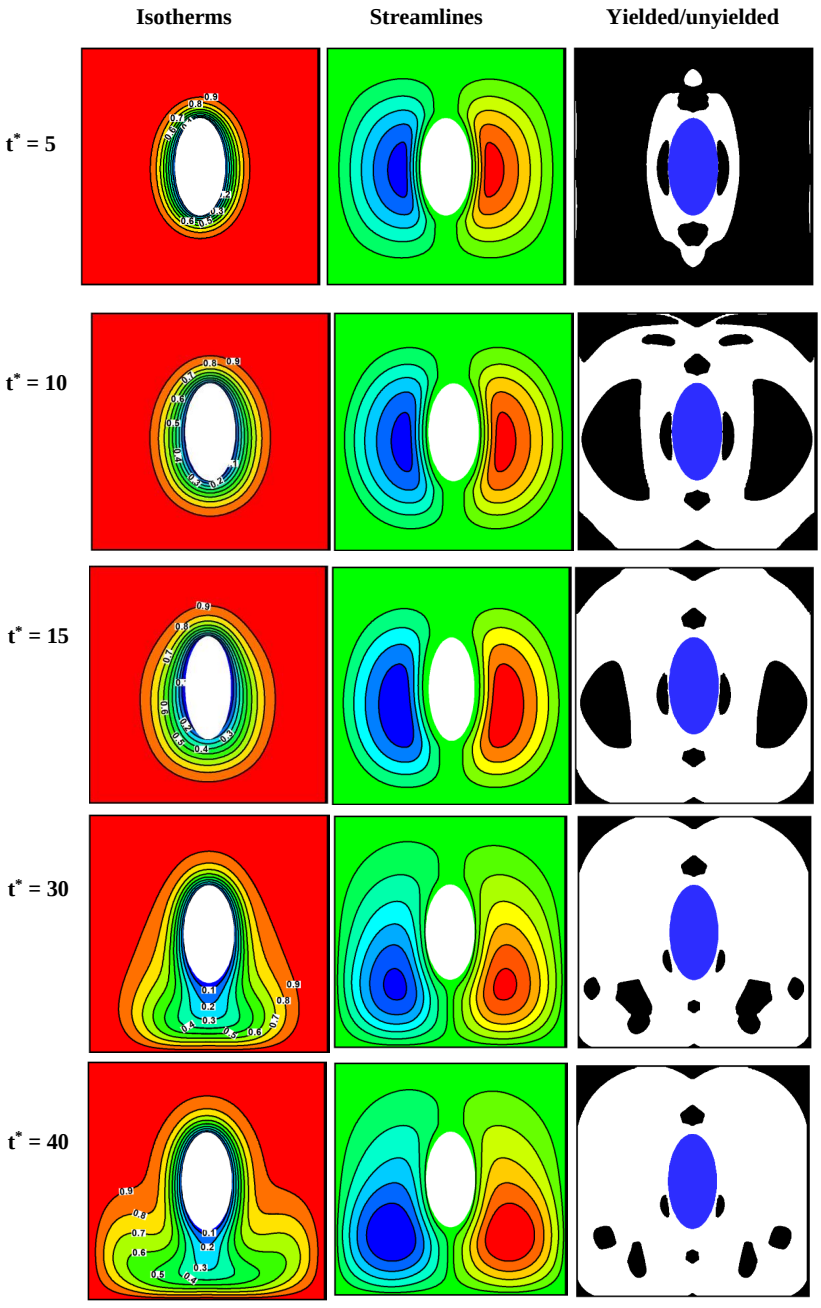

Fig. 3. The comparison of the isotherms, streamlines and yielded/unyielded parts in different non-dimensional time (t^*) at $x_c = y_c = 0.5$ L, Bn = 7, Ec = 0, $\theta = 0°$, and a = 0.1 L, b = 0.2 L

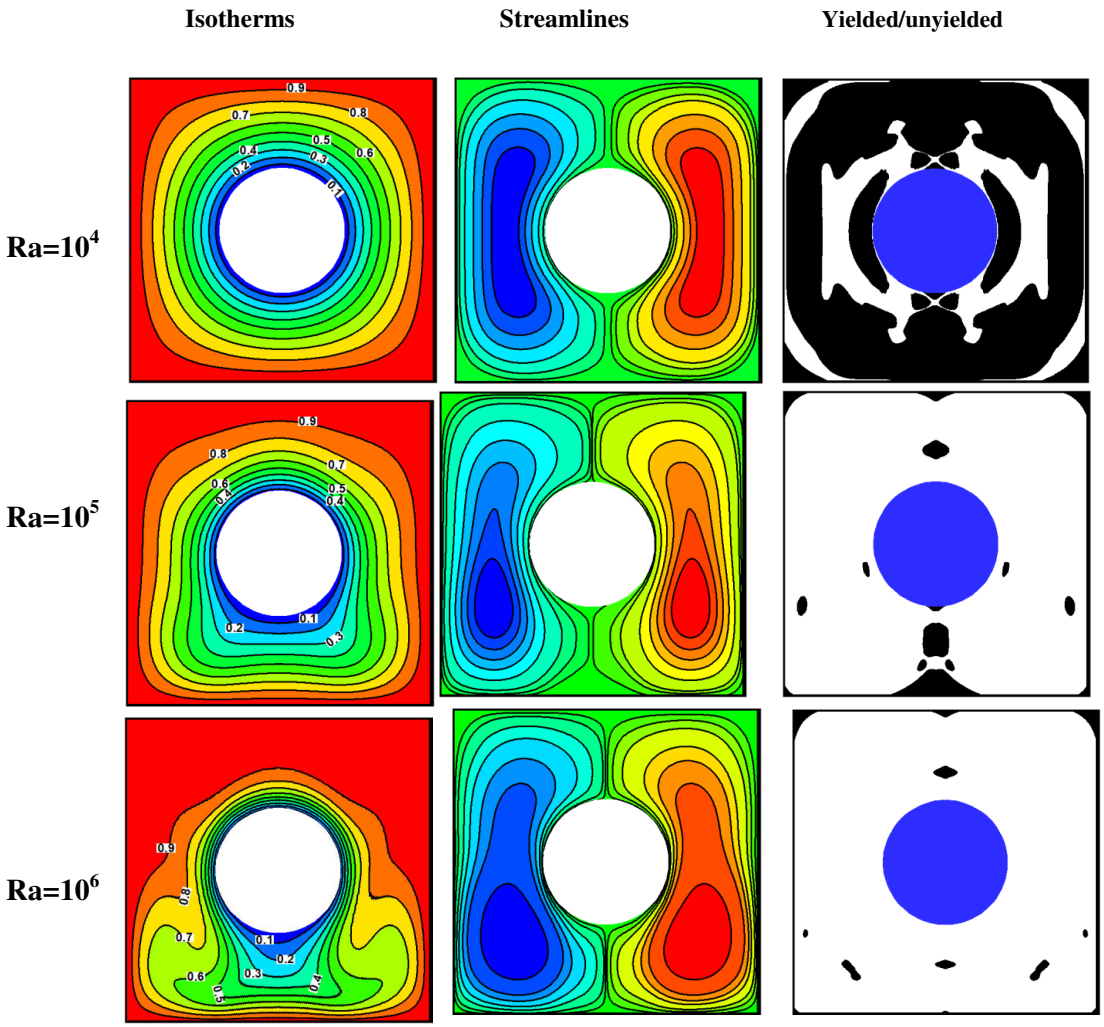

Fig. 4. The comparison of the isotherms, streamlines and yielded/unyielded parts in different Rayleigh numbers at $x_c = y_c = 0.5$ L, Bn = 1, Ec = 0, $\theta = 0°$, and a = b = 0.2 L

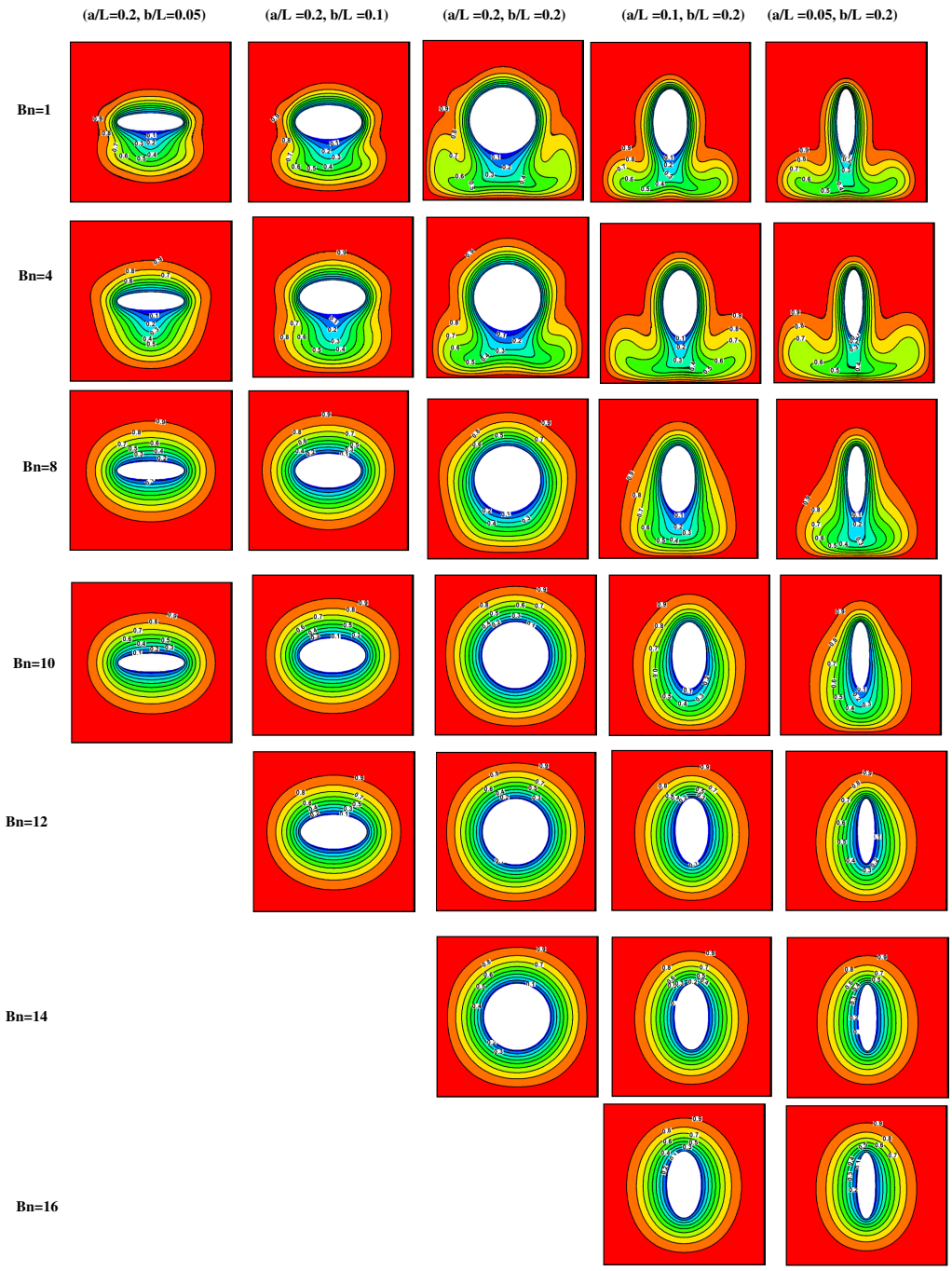

Fig. 5. The comparison of the isotherms in different radii and Bingham numbers at $x_c = y_c = 0.5$ L, Ra $= 10^6$, Ec $= 0$, and $\theta = 0^\circ$

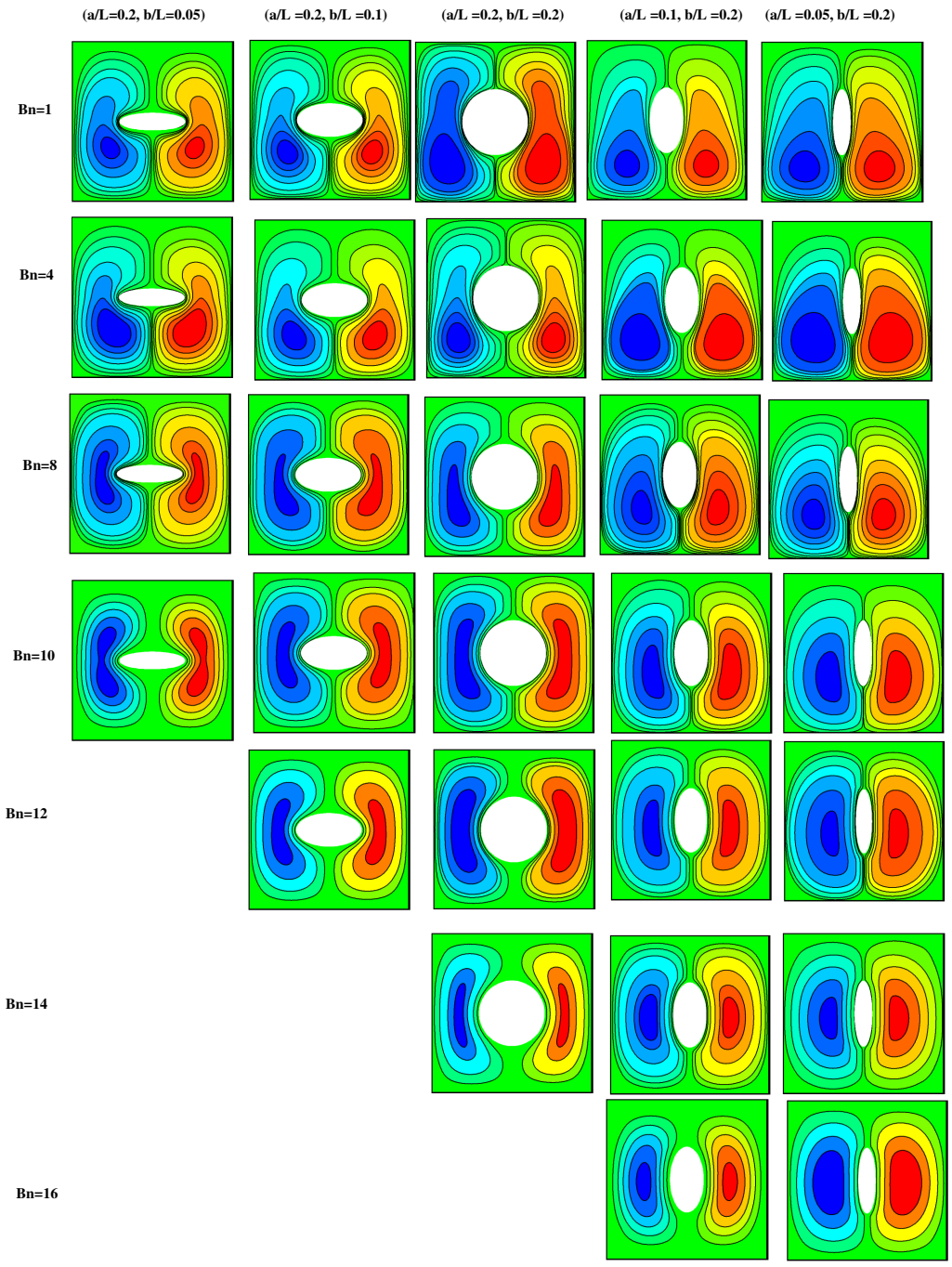

Fig. 6. The comparison of the streamlines in different radii and Bingham numbers at $x_c = y_c = 0.5$ L, Ra $= 10^6$, Ec $= 0$, and $\theta = 0^\circ$

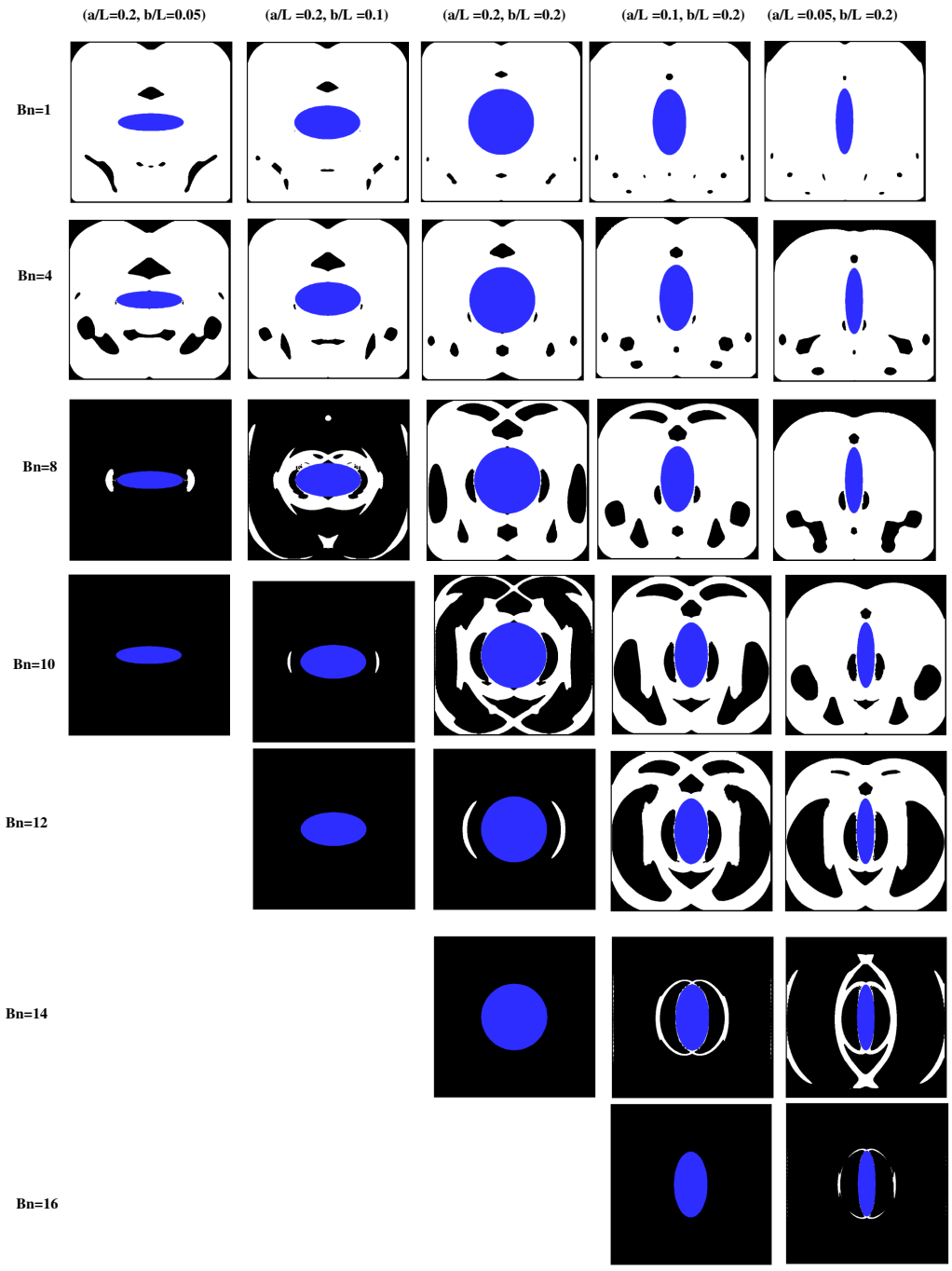

Fig. 7. The comparison of the yielded/unyielded zones in different radii and Bingham numbers at $x_c = y_c = 0.5$ L, Ra $= 10^6$, Ec $= 0$, and $\theta = 0^\circ$

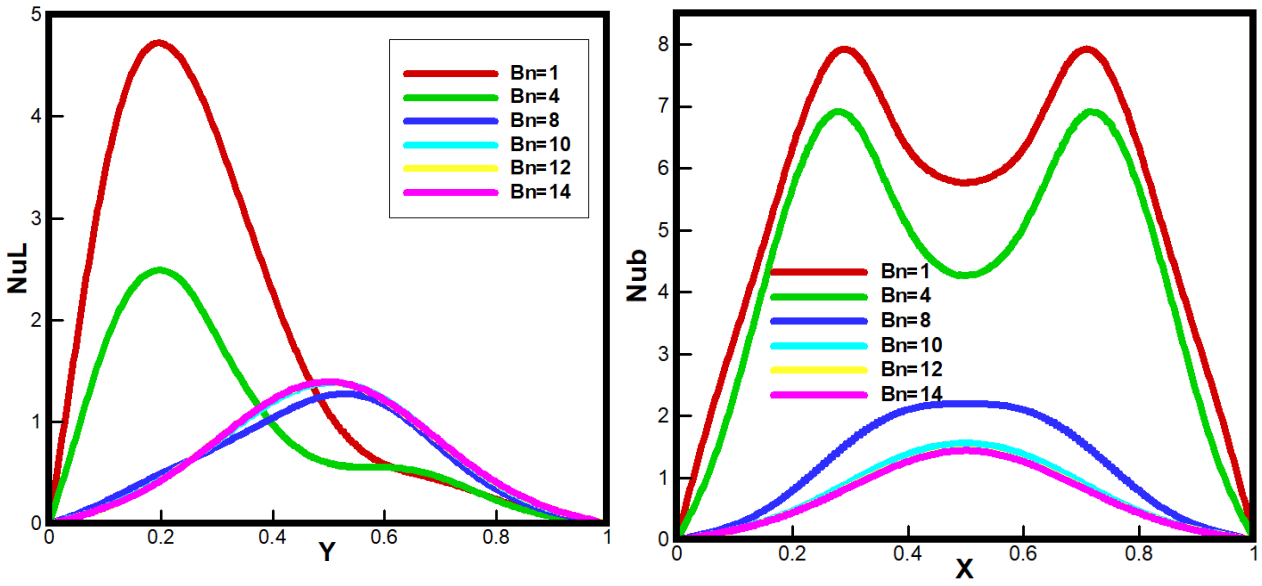

Fig. 8. The local Nusselt numbers on the left wall (Nu_L) and the bottom wall (Nu_b) in different Bingham numbers at $x_c = y_c = 0.5$ L, Ra $= 10^6$, Ec $= 0$, $\theta = 0°$, and a $=$ b $= 0.2$ L

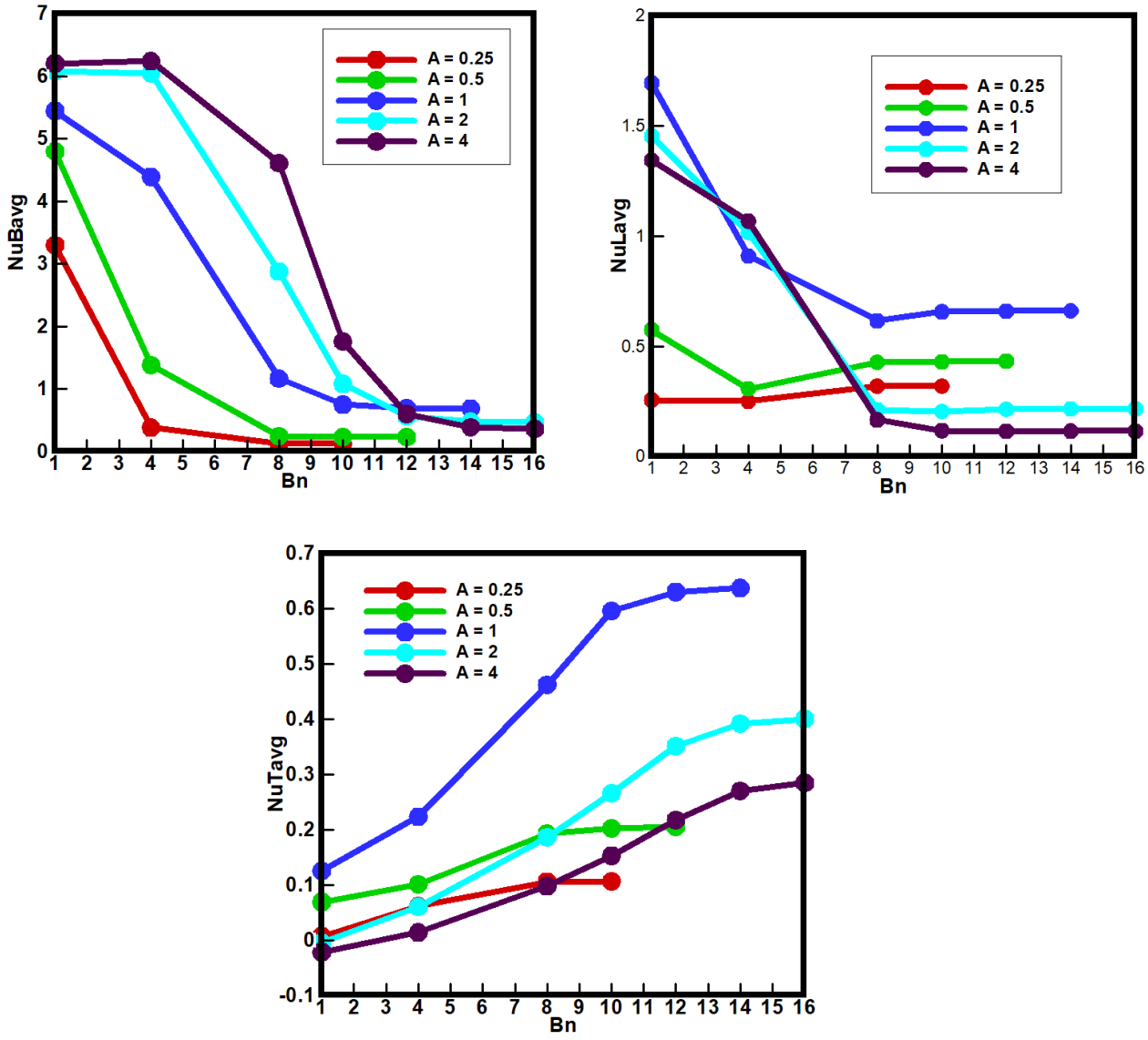

Fig. 9. The average Nusselt numbers on the top wall (Nu_{Tavg}), the left wall (Nu_{Lavg}) and the bottom wall (Nu_{Bavg}) in different Bingham numbers and aspect ratios of the radii at $x_c = y_c = 0.5$ L, Ra $= 10^6$, Ec $= 0$, $\theta = 0°$

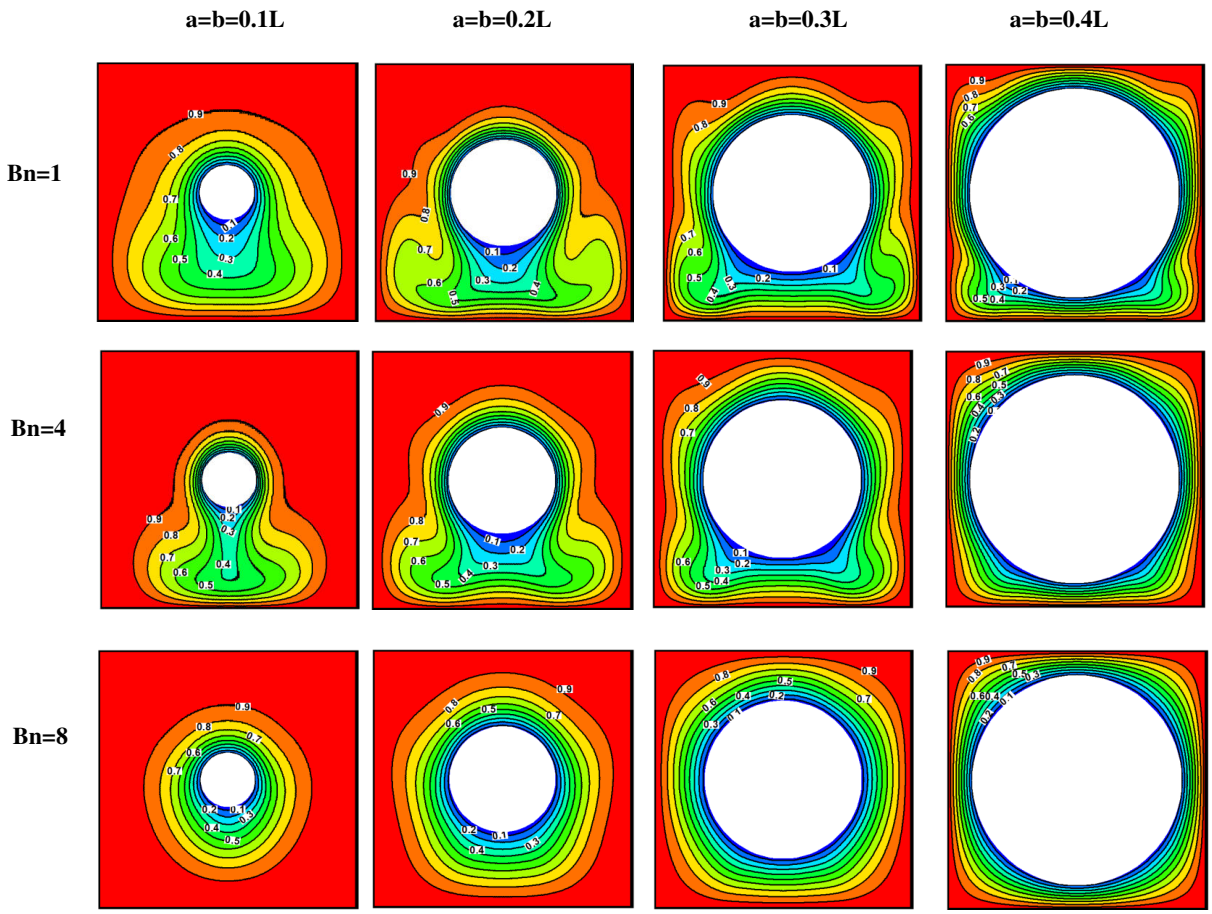

Fig. 10. The comparison of the isotherms in different sizes and Bingham numbers at $x_c = y_c = 0.5$ L, Ra $= 10^6$, Ec=0, and $\theta = 0°$

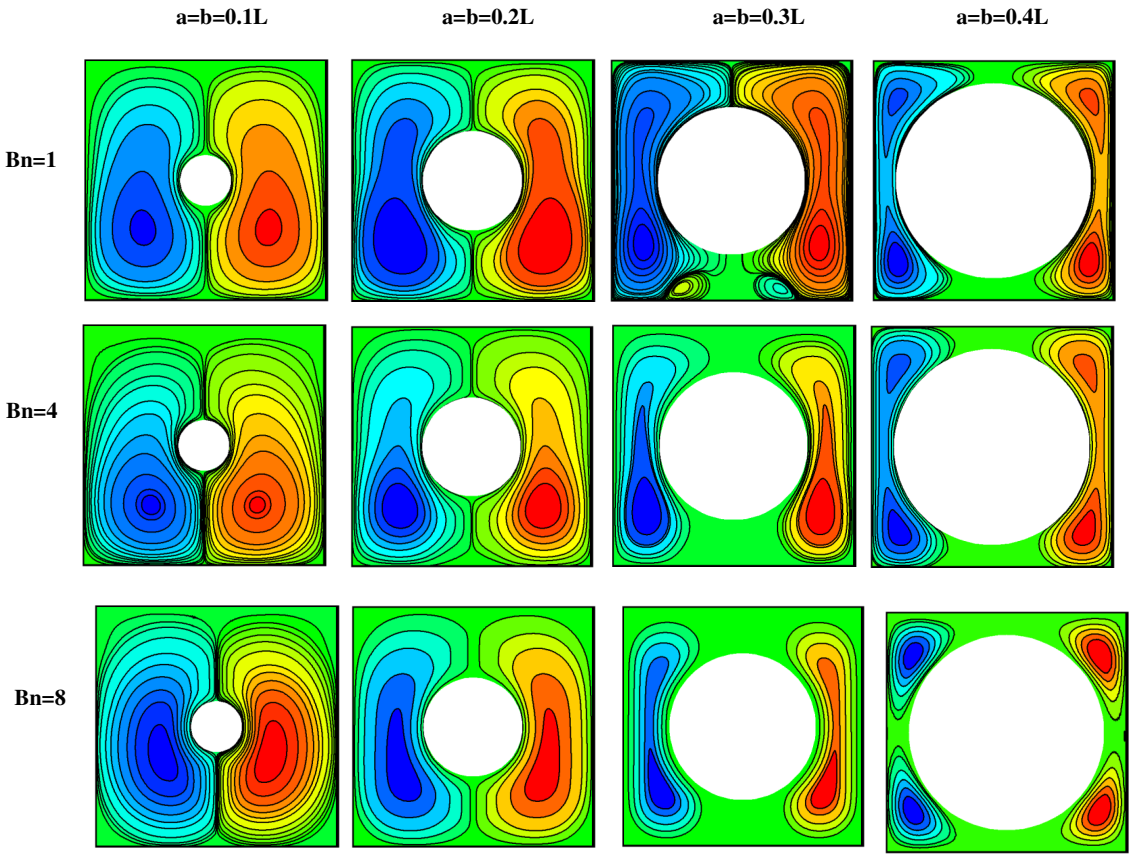

Fig. 11. The comparison of the streamlines in different sizes and Bingham numbers at $x_c = y_c = 0.5$ L, Ra $= 10^6$, Ec $= 0$, and $\theta = 0^\circ$

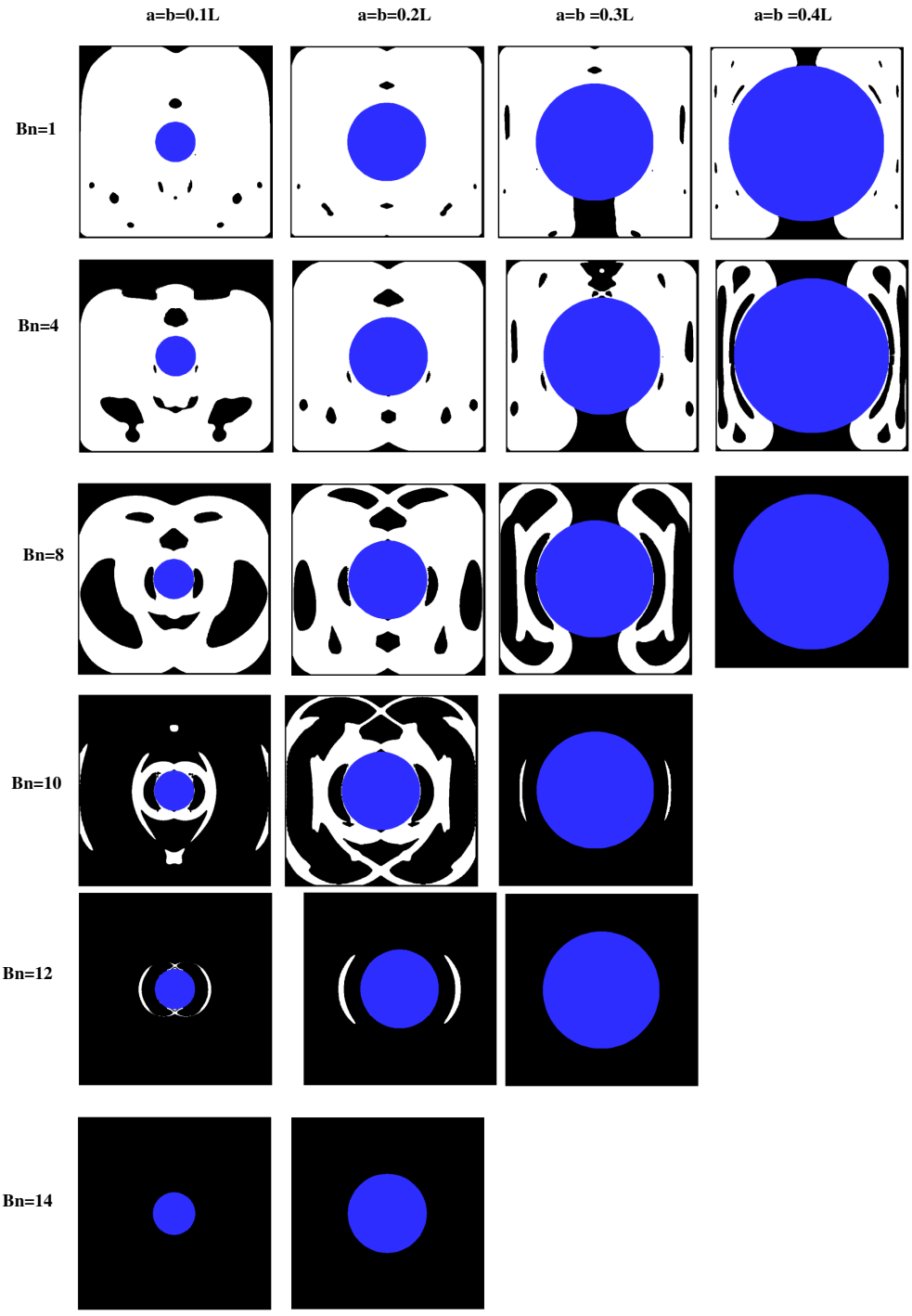

Fig. 12. The comparison of the yielded/unyielded zones in different sizes and Bingham numbers at $x_c = y_c = 0.5$ L, Ra $= 10^6$, Ec $= 0$, and $\theta = 0^\circ$

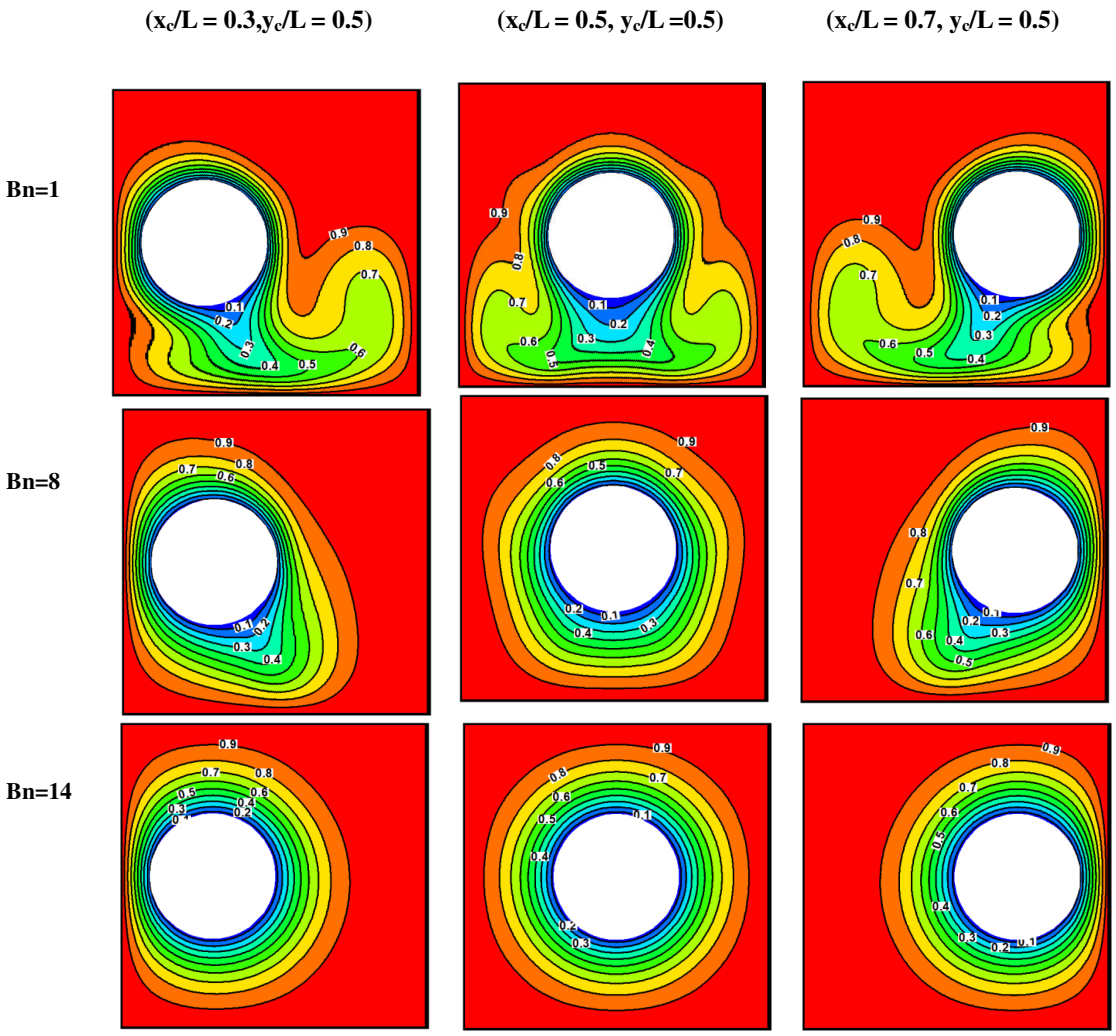

Fig. 13. The comparison of the isotherms in different horizontal positions and Bingham numbers at y_c = 0.5 L, Ra = 10^6, Ec = 0, and a = b = 0.2 L, and $\theta = 0°$

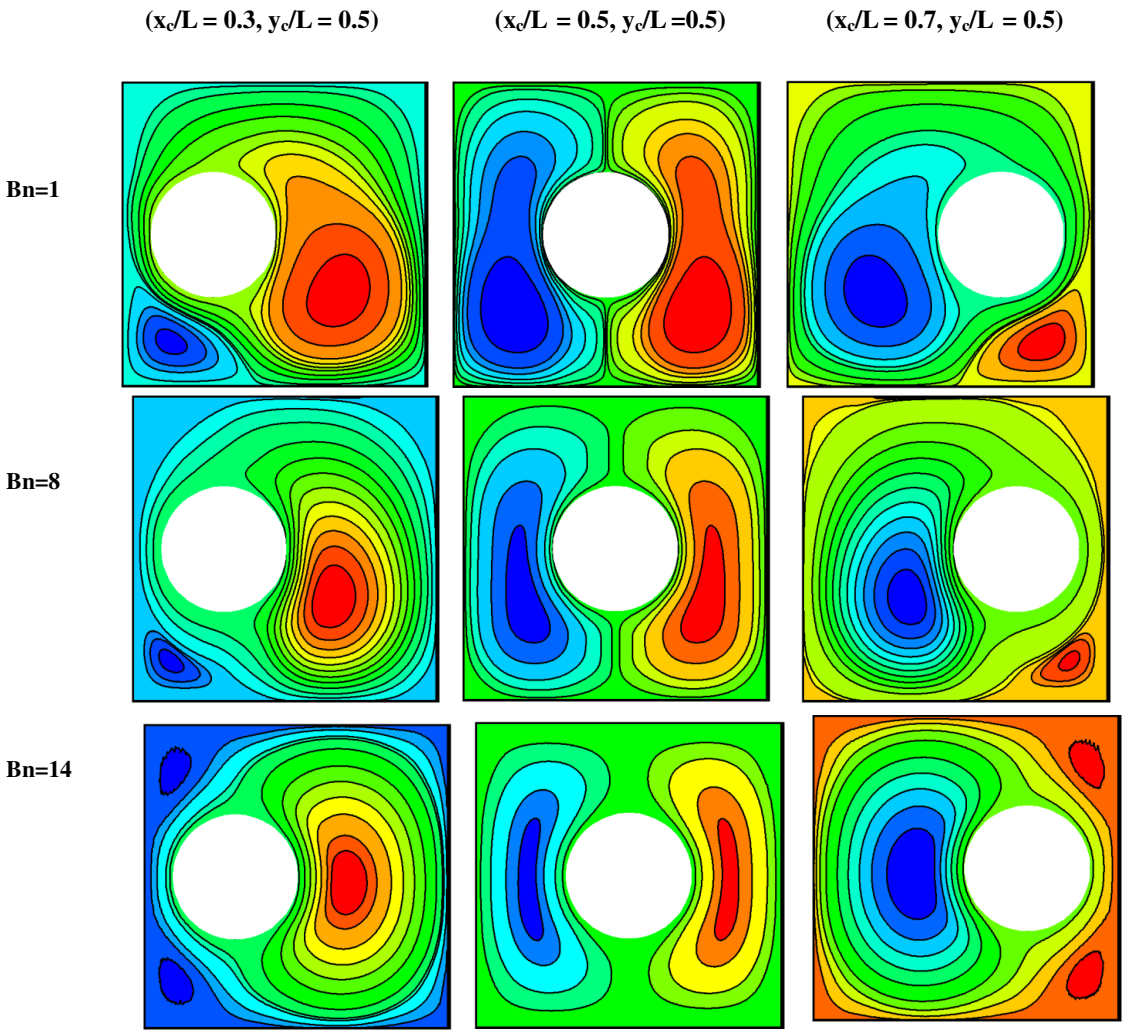

Fig. 14. The comparison of the streamlines in different horizontal positions and Bingham numbers at $y_c = 0.5$ L, Ra $= 10^6$, Ec $= 0$, and a $=$ b $= 0.2$ L, and $\theta = 0°$

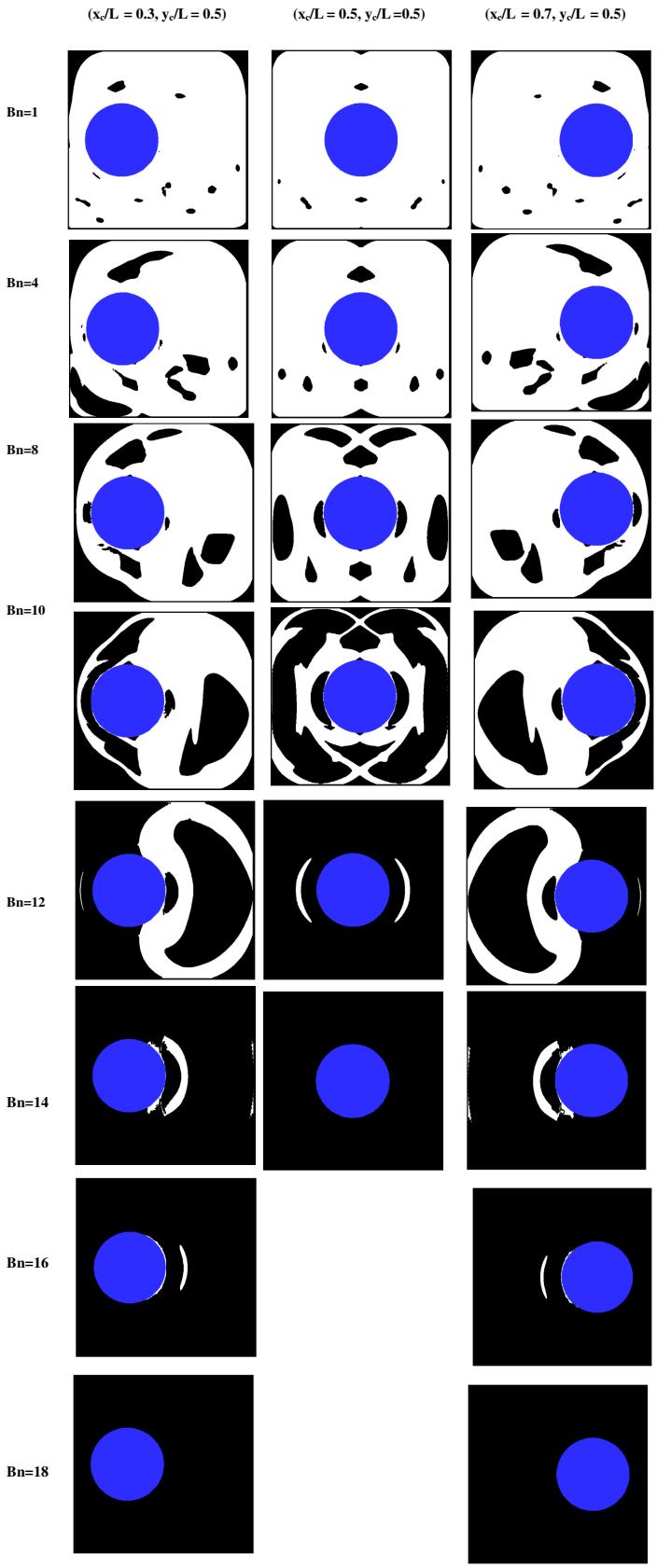

Fig. 15. The comparison of the yielded/unyielded zones in different horizontal positions and Bingham numbers at $y_c = 0.5$L, Ra $= 10^6$, Ec $= 0$, and a $=$ b $= 0.2$ L, and $\theta = 0^\circ$

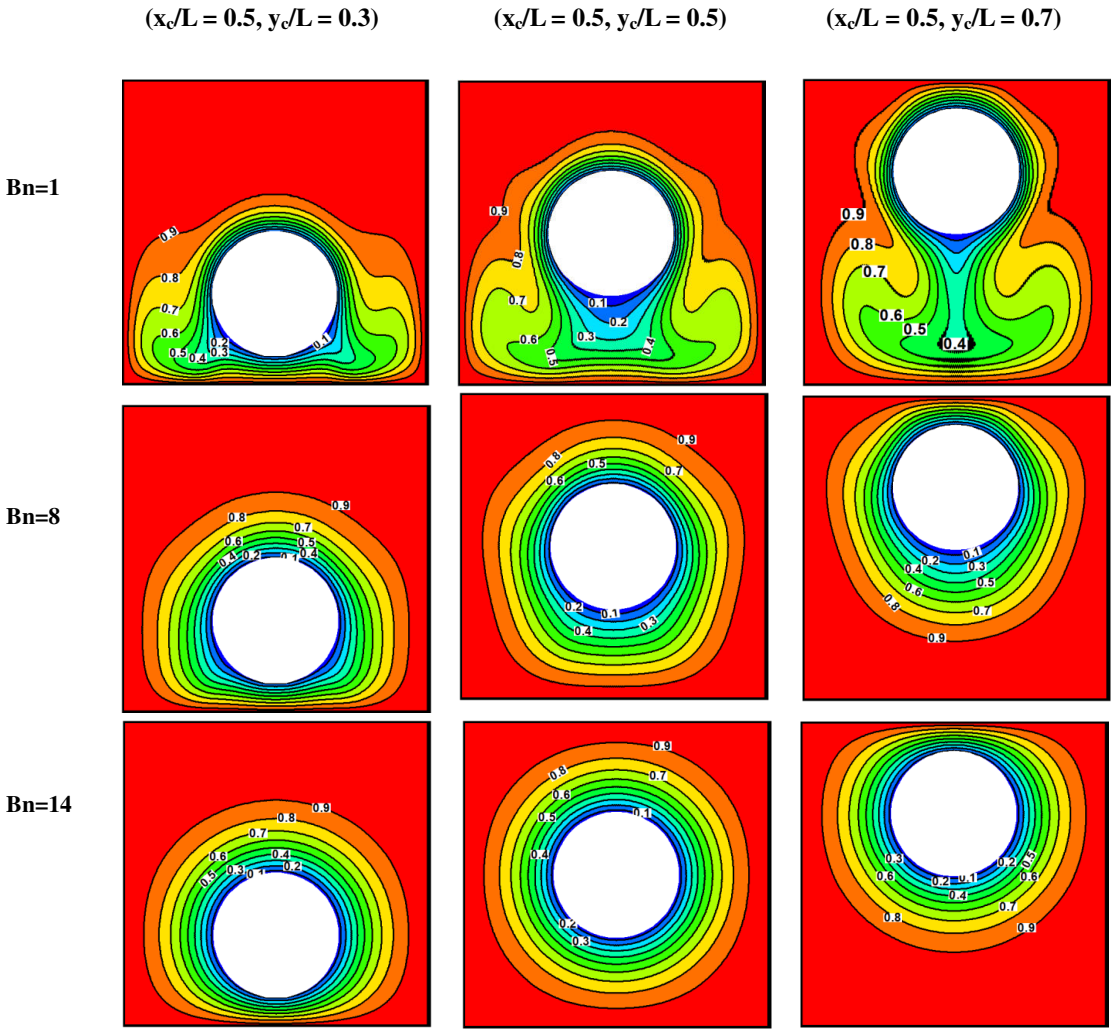

Fig. 16. The comparison of the isotherms in different vertical positions and Bingham numbers at x_c = 0.5 L, Ra = 10^6, Ec = 0, and a = b = 0.2 L, and $\theta = 0°$

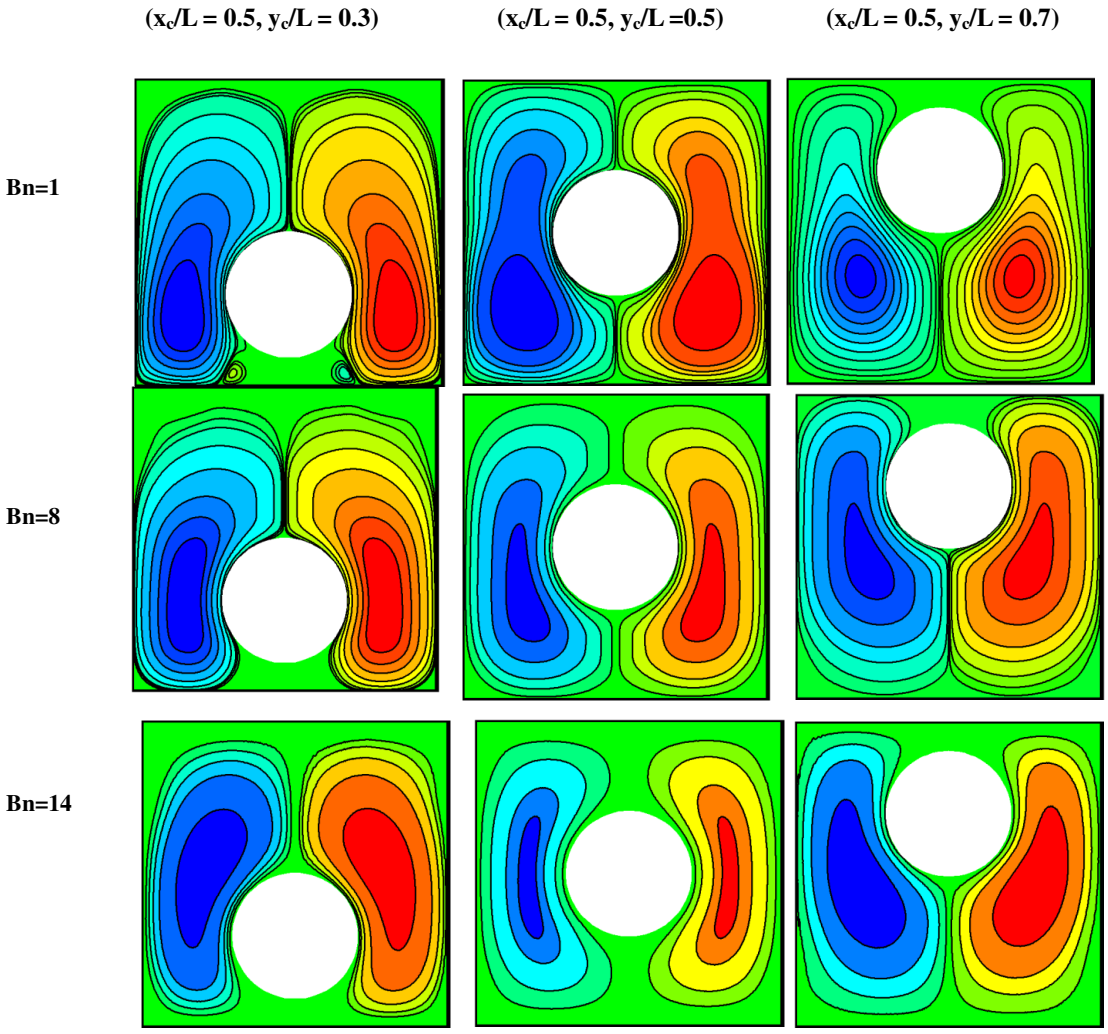

Fig. 17. The comparison of the streamlines in different vertical positions and Bingham numbers at x_c = 0.5 L, Ra = 10^6, Ec = 0, and a = b = 0.2 L, and $\theta = 0°$

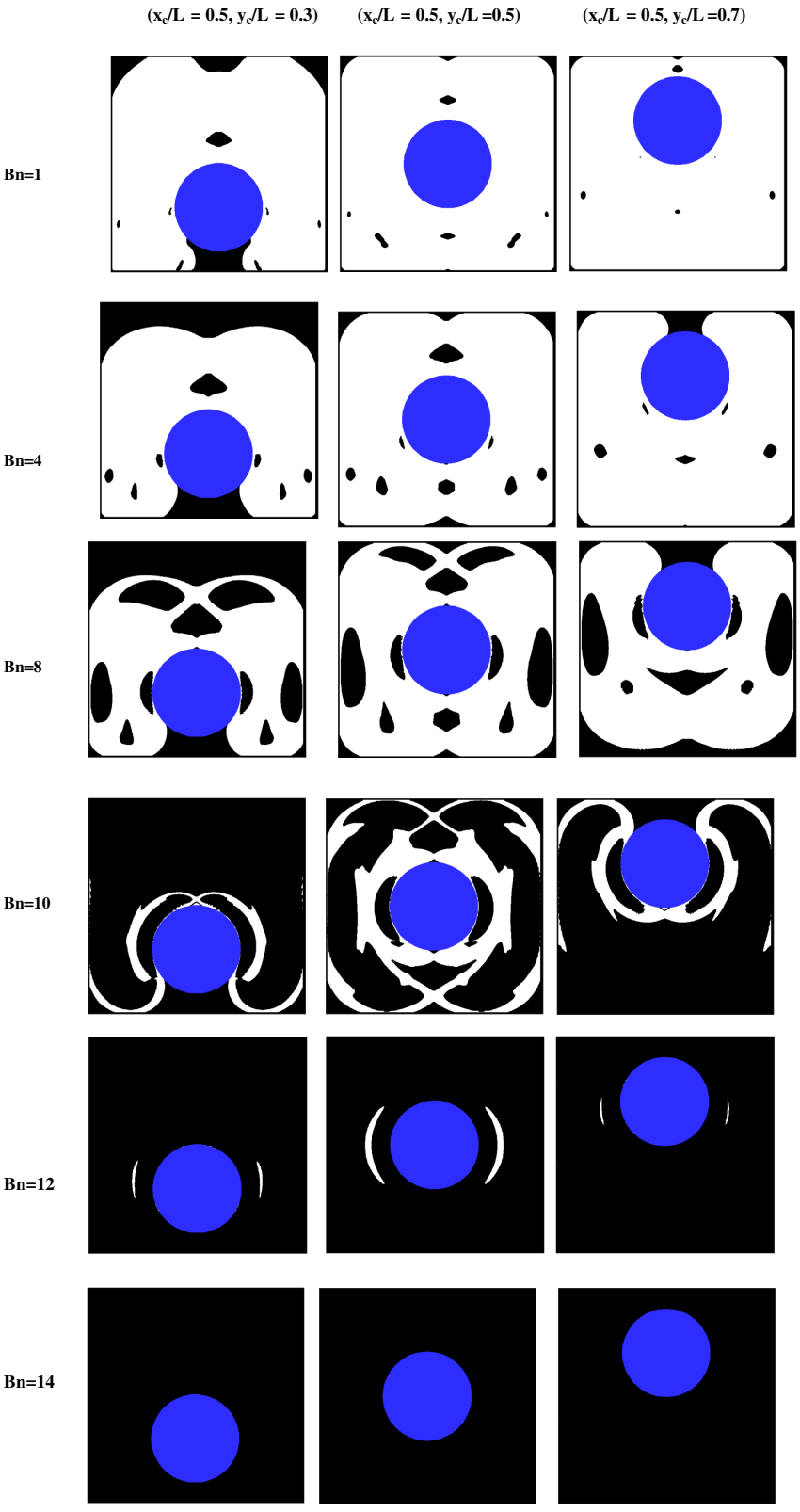

Fig. 18. The comparison of the yielded/unyielded zones in different vertical positions and Bingham numbers at x_c = 0.5 L, Ra = 10^6, Ec = 0, and a = b = 0.2 L, and $\theta = 0^\circ$

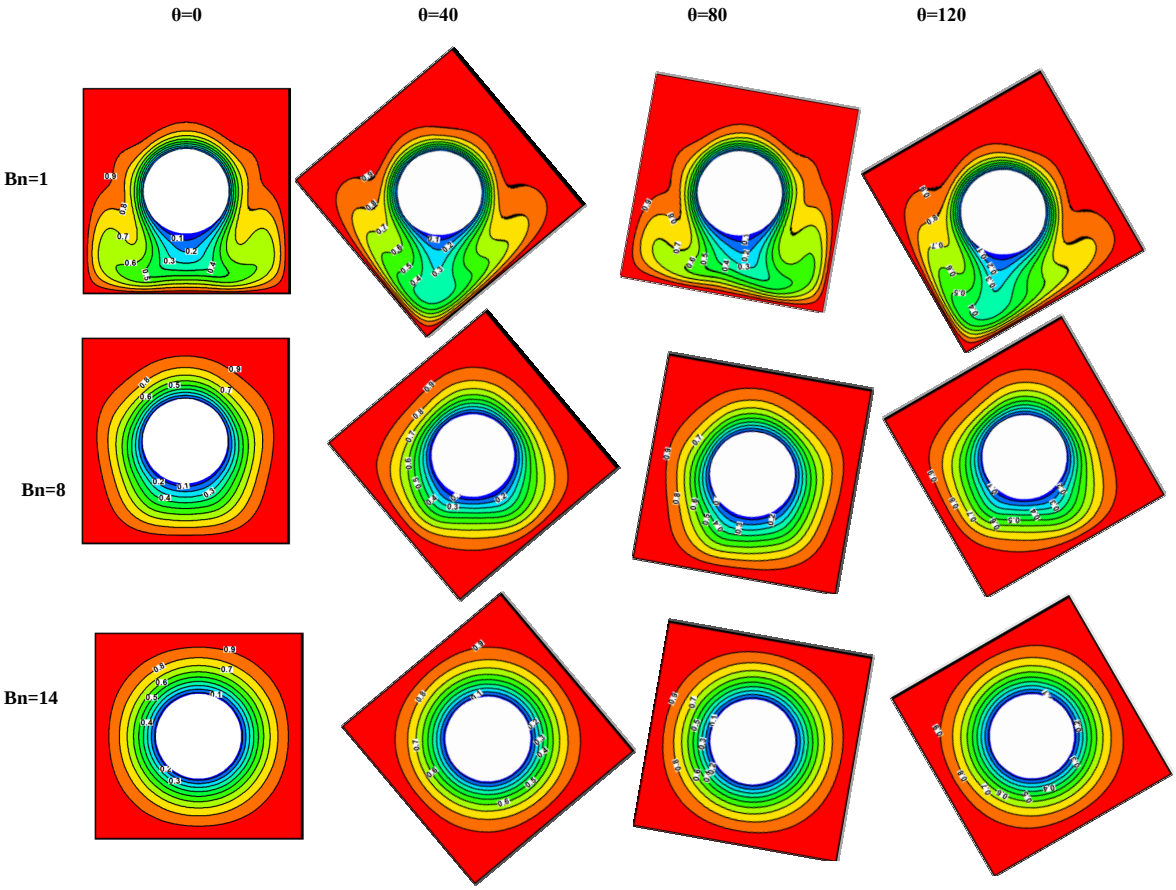

Fig. 19. The comparison of the isotherms in different inclined angles and Bingham numbers at $x_c = y_c = 0.5$ L, Ra $= 10^6$, Ec $= 0$, and a $=$ b $= 0.2$ L

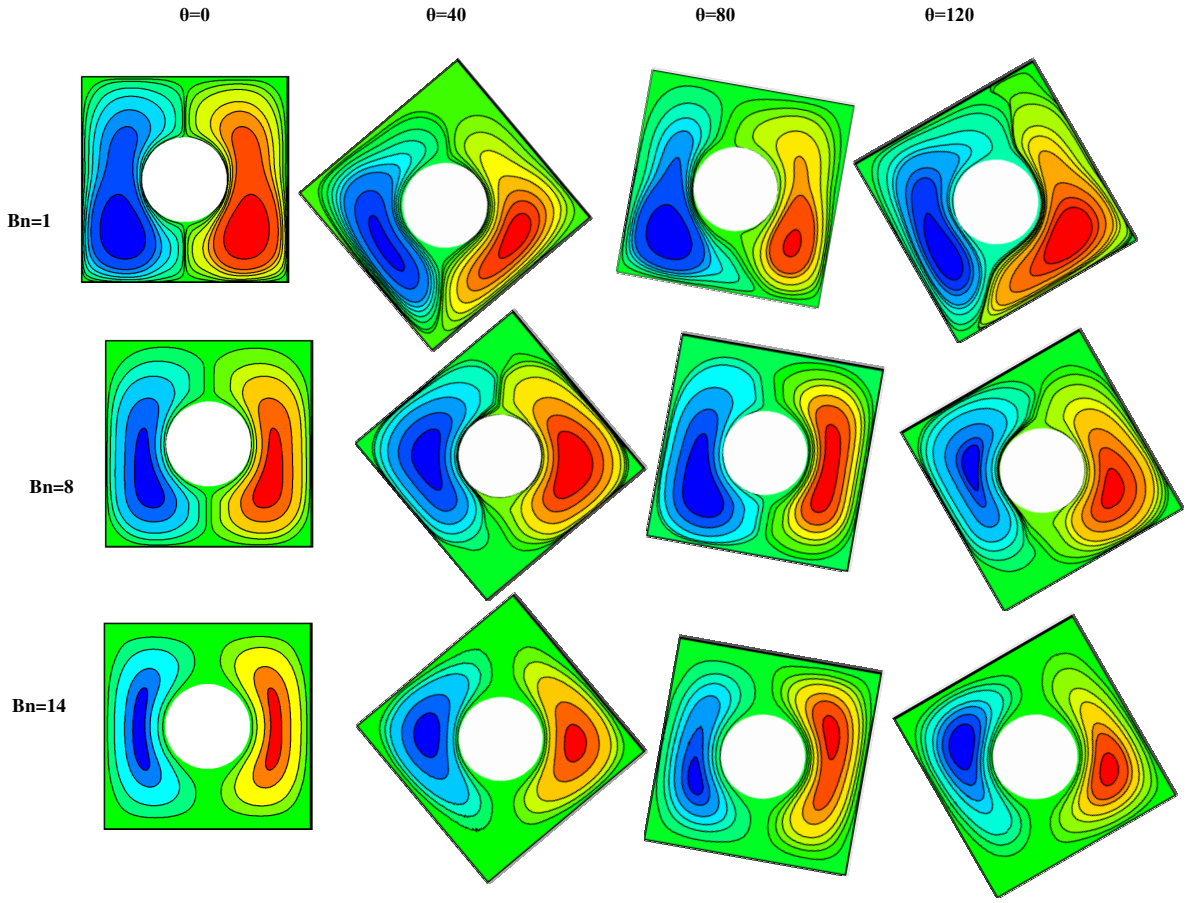

Fig. 20. The comparison of the streamlines in different inclined angles and Bingham numbers at $x_c = y_c = 0.5$ L, Ra $= 10^6$, Ec $= 0$, and a $=$ b $= 0.2$ L

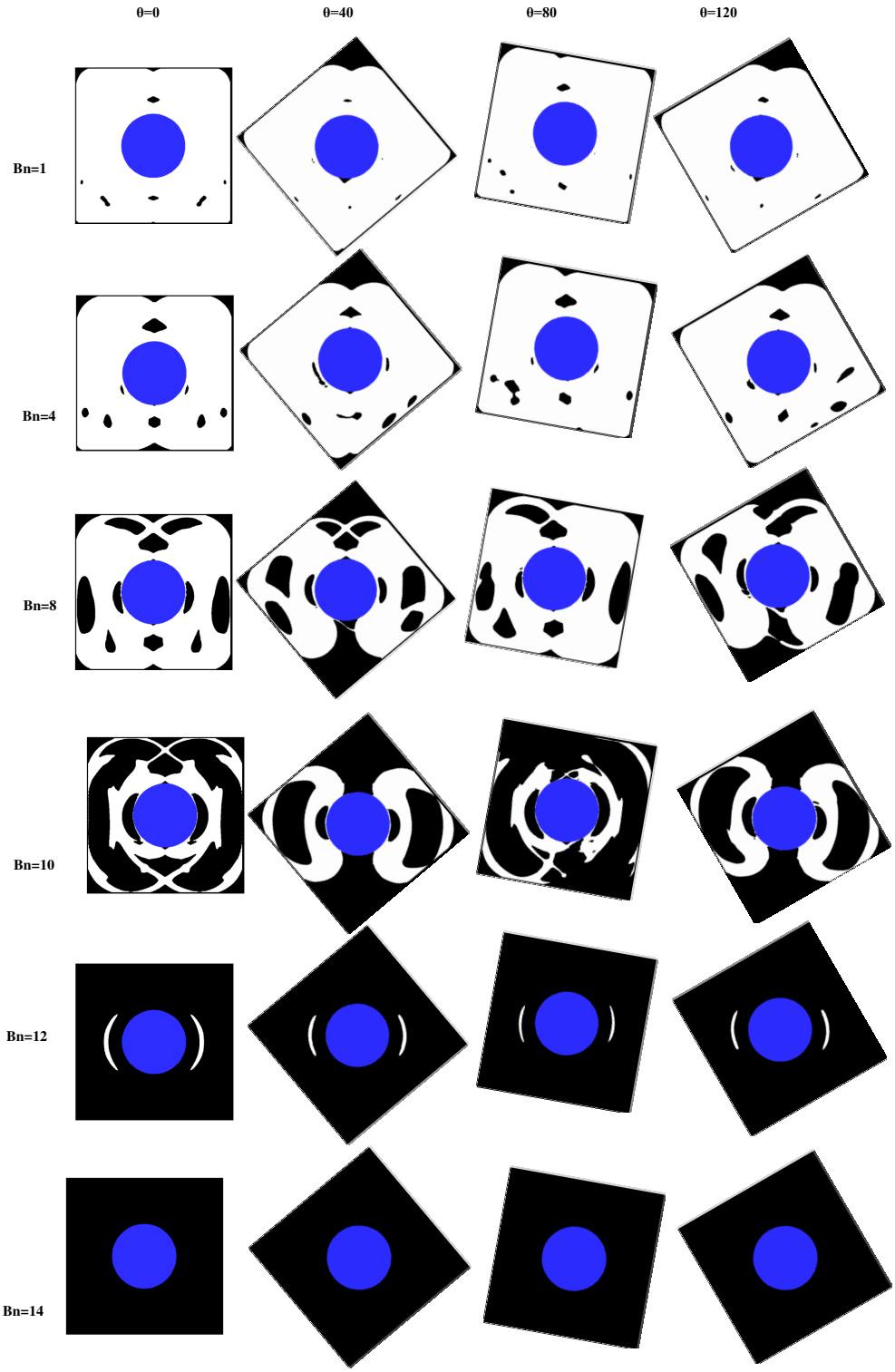

Fig. 21. The comparison of the yielded/unyielded zones in different inclined angles and Bingham numbers at $x_c = y_c = 0.5$ L, Ra $= 10^6$, Ec $= 0$, and a $=$ b $= 0.2$ L

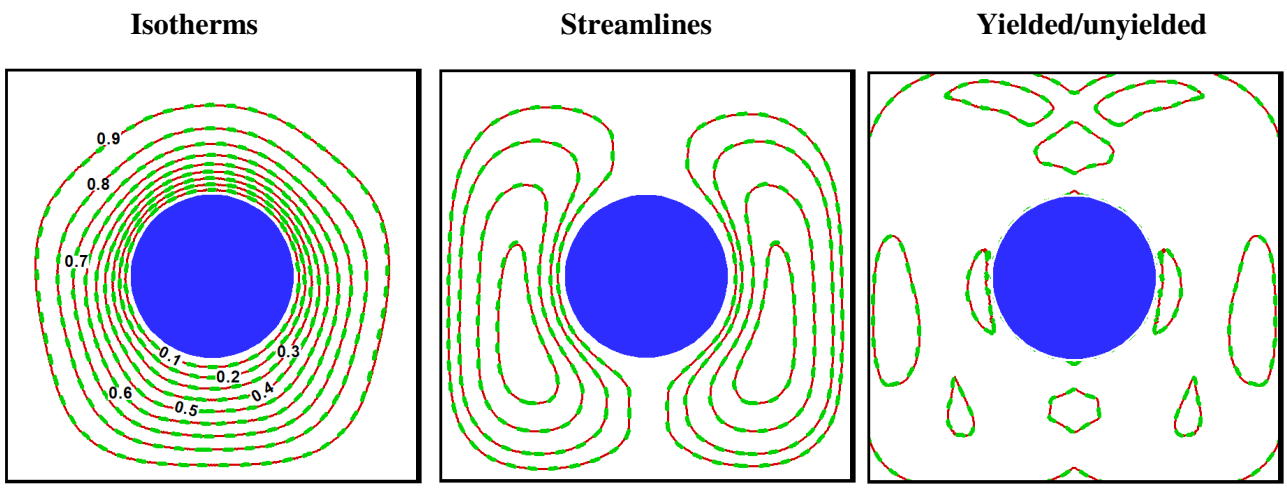

Fig. 22. The comparison of the isotherms, streamlines and yielded/unyielded parts in different Eckert numbers (Ec = 0 (red line) and Ec = 1 (dashed green line)) at $x_c = y_c = 0.5$ L, Bn = 8, and a = b = 0.2 L, and $\theta = 0^\circ$